

Numerical investigation of the interaction of the Klebanoff-mode with a Tollmien–Schlichting wave

By HERMANN F. FASEL

Department of Aerospace and Mechanical Engineering,
University of Arizona, Tucson, AZ 85721, USA

(Received 3 June 1997 and in revised form 7 June 2001)

Direct numerical simulations (DNS) of the Navier–Stokes equations are used to investigate the role of the Klebanoff-mode in laminar–turbulent transition in a flat-plate boundary layer. To model the effects of free-stream turbulence, volume forces are used to generate low-frequency streamwise vortices outside the boundary layer. A suction/blowing slot at the wall is used to generate a two-dimensional Tollmien–Schlichting (TS) wave inside the boundary layer. The characteristics of the fluctuations inside the boundary layer agree very well with those measured in experiments. It is shown how the interaction of the Klebanoff-mode with the two-dimensional TS-wave leads to the formation of three-dimensional TS-wavepackets. When the disturbance amplitudes reach a critical level, a fundamental resonance-type secondary instability causes the breakdown of the TS-wavepackets into turbulent spots.

1. Introduction

In the ‘classical’ view, laminar–turbulent transition in a boundary layer on a flat plate in a low-disturbance environment is seen as the result of four distinct processes (Morkovin 1993): receptivity – linear instability – secondary instability – breakdown.

In the first stage, receptivity, disturbance waves in the boundary layer are excited by external perturbations such as surface roughness, surface vibrations, sound waves, free-stream turbulence (FST), or unsteady pressure gradients.

Beyond a certain critical Reynolds number Re_{cr} , disturbance waves inside the boundary layer may become amplified due to a linear instability of the steady mean flow. These amplified waves are called Tollmien–Schlichting (TS) waves. When the amplitude of a TS-wave has reached a sufficiently high level, the TS-wave and the steady mean flow together can be thought of as a new base flow. In a coordinate system that moves with the phase speed of the TS-wave, this base flow is approximately steady in time but periodic in the streamwise direction x . This periodic base flow becomes susceptible to a Floquet-type secondary instability (Craik 1971; Herbert 1988). This instability gives rise to disturbances which are typically oblique (i.e. with non-zero spanwise wavenumber). At this stage, disturbance growth becomes so strong that turbulent spots and breakdown to turbulence occur within a short streamwise distance.

The major shortcoming of the above transition scenario is that it can only be observed in carefully controlled experiments, i.e. in specially designed wind and water tunnels where free-stream turbulence, ambient noise, and vibrations have been

reduced to a minimum. Whether this route to turbulence is prevalent in free flight is an unresolved issue. Under ‘natural’ conditions found in wind tunnels with FST levels $Tu > 0.1\%$, transition appears to be preceded by streamwise streaks in the boundary layer. These streaks are now commonly referred to as the ‘Klebanoff-mode’ (or K-mode), after P. S. Klebanoff who first described them (Klebanoff & Tidstrom 1959; Klebanoff 1971). His basic findings have been confirmed in numerous experiments by other researchers (Arnal & Juillen 1978; Kendall 1985, 1990, 1992; Westin *et al.* 1994; Boiko *et al.* 1994).

The streamwise streaks associated with the K-mode are fundamentally different both from TS-waves and from the structures commonly observed in turbulent boundary layers. They are longitudinal structures inside the boundary layer that appear to be caused by free-stream turbulence. Characteristic features of the K-mode are its low frequency and its high amplitude. Fluctuations as high as $u_{rms}/U_\infty = 15\%$ have been recorded in boundary layers before the appearance of turbulence. This is in strong contrast to the amplitudes commonly observed in TS-waves, where values of $u_{rms}/U_\infty \approx 1.5\%$ are usually an indication of imminent transition to turbulence. Also in contrast to the exponential growth of TS-waves, in most experiments the amplitude of the K-mode increases algebraically in the streamwise direction, being roughly proportional to \sqrt{x} . The structures are long in the streamwise direction and narrow in the spanwise direction, with a characteristic spanwise length scale (in this paper the spanwise wavelength is used) of a few boundary layer thicknesses $\delta_{99\%}$ of the unperturbed boundary layer. At present there is no consensus on whether this spanwise scale is imposed by the scale of the free-stream turbulence or whether it is an intrinsic scale of the boundary layer. In the wall-normal direction the structures extend across the whole boundary layer.

To date, there is no comprehensive theory concerning the origin and streamwise development of the K-mode. There have been several theoretical studies of the development of steady spanwise perturbations in a Blasius boundary layer. Crow (1966) used an asymptotic expansion to study the response of a Blasius boundary layer to steady spanwise perturbations of the free-stream velocity $U(z) = U_\infty(1 + \epsilon \sin(\gamma z))$. Within the limits of his analysis, $v\gamma/U_\infty \ll \gamma x \ll U_\infty/v\gamma$, he found that the spanwise variation of the boundary layer thickness was proportional to ϵk . Goldstein and coworkers used numerical solutions of the three-dimensional boundary layer equations to investigate the effects of steady normal (Goldstein, Leib & Cowley 1992) and spanwise (Goldstein & Leib 1993) free-stream perturbations on boundary layers. In both cases they found strong growth of steady spanwise distortions inside the boundary layer which eventually caused the boundary layer to separate. Bertolotti (1993), using the parabolized stability equations (PSE), found that, in the absence of free-stream perturbations and any other forcing, steady vortices decayed in a Blasius boundary layer.

The role of the K-mode in laminar–turbulent transition is still not understood. When the FST level is increased, the amplitude of the K-mode increases as well, and the transition to turbulence occurs farther upstream in the boundary layer. There is, however, no clear link between the K-mode and any known instability or transition mechanism. Because of the intensity of the overall fluctuations, it is quite difficult to measure the amplitudes of TS-waves in the presence of the K-mode. Kendall (1992) reported that naturally occurring TS-waves appeared in the form of wavepackets. Their growth depended on their amplitude, and their spanwise extent appeared to be related to the spanwise scale of the K-mode. These characteristics are in contrast to those of artificial wavepackets in an otherwise quiescent boundary layer, whose growth

and spanwise spreading is described well by linear stability theory (Gaster & Grant 1975). Boiko *et al.* (1994) artificially excited a time-harmonic two-dimensional TS-wave with a vibrating ribbon in the presence of free-stream turbulence. They showed that artificial excitation of TS-waves had a strong effect on transition. An increase in the forced TS-amplitude lead directly to an increase in the number of turbulent spots observed further downstream, and caused transition to occur earlier. However, they also found that the ensemble-averaged growth rates of the artificially induced two-dimensional TS-waves were smaller than predicted by theory (for a Blasius boundary layer without the K-mode), and that an increase of the K-mode amplitude resulted in a decrease of the TS-wave growth rates. These findings, seemingly contradictory, point to the important role that is played by intermittency in this transition route.

2. Scope of the present work

In this study an attempt is made to model the effects of free-stream turbulence on the K-mode, and subsequently on transition, in a flat-plate boundary layer. It should be stated at the outset that this work is not intended to be a complete direct numerical simulation of the evolution of free-stream turbulence in the presence of a boundary layer, and of its influence on transition inside the boundary layer. Such a simulation would have to capture a wide band of wavenumbers and frequencies, requiring hundreds of grid points in all three spatial directions and thousands of time steps. It would reach the limits of today's most powerful computers, without necessarily providing more physical insight than a simplified model. However, such a simulation may be necessary to obtain complete quantitative agreement with experiments.

Here, the goal is to find a numerical model that is sufficiently simplified to allow practical simulations, yet realistic enough to capture the relevant physical mechanism. A review of the available experimental results can serve as a starting point to determine what should be included in (or reproduced by) such a model. All experimental reports agree on certain characteristics of the K-mode fluctuations inside flat-plate boundary layers (Arnal & Juillen 1978; Kendall 1985, 1990, 1992; Westin *et al.* 1994):

- (i) very low frequencies compared to TS-waves;
- (ii) distinct spanwise scaling, $O(2\delta_{99\%} - 4\delta_{99\%})$;
- (iii) streamwise growth proportional to \sqrt{x} ;
- (iv) high amplitudes $u_{rms} = O(10\%U_\infty)$.

The strong response of the boundary layer appears to be limited to a narrow band of the wavenumber–frequency spectrum. Furthermore, the growth of the disturbances (algebraic, instead of, say, exponential) suggests that the receptivity of the boundary layer to free-stream turbulence is distributed, rather than concentrated at the leading edge or at a surface imperfection. Also, if the free-stream turbulence is sufficiently homogeneous, the combined effects of most turbulent eddies on the boundary layer would tend to cancel each other. Then, due to the rapid decay of the velocity induced by turbulent eddies farther away from the wall, most of the influence of free-stream turbulence on the boundary layer would come from those eddies that are closest to the edge of the boundary layer.

These considerations suggest the following approach to a simplified numerical model for the generation of the K-mode. Low-frequency volume forces are used to generate unsteady vortices in the free stream. The volume forces are concentrated near the leading edge of the plate, between the edge of the boundary layer and the free-stream boundary. The details of the forcing algorithm are given in §3. This forcing generates long, narrow, streamwise vortices. Once generated, the vortices are swept

downstream by the free stream, and they are sufficiently attenuated inside the buffer domain (see §3) so that they do not cause any reflections at the outflow boundary. Also, this method of generating free-stream vortices ensures that no vorticity reaches the inflow or free-stream boundaries. While the vortices are exponentially damped in the downstream direction, they cause spanwise perturbations of the free-stream velocity, which in turn continuously force the boundary layer. To assess the validity and accuracy of the numerical model, the response of the boundary layer to these unsteady free-stream vortices in the numerical simulations is compared to the response of boundary layers to ‘real’ free-stream turbulence measured in experiments. Good qualitative (and quantitative) agreement between the numerical and experimental results can be considered as a validation and confirmation of the numerical model.

In this paper the results of several numerical simulations are presented. In §4, the linear and nonlinear evolution of a flat-plate boundary layer subject to steady and low-frequency free-stream vortices is investigated. First, the results of simulations using the linearized Navier–Stokes equations are presented. These results provide the necessary information for the selection of the appropriate wavenumber–frequency combinations for later, nonlinear calculations. They also serve as benchmarks to determine the correct forcing amplitudes to obtain a desired fluctuation level inside the boundary layer. Next, the effects of high-amplitude, unsteady free-stream vortices on a boundary layer are calculated using the full nonlinear Navier–Stokes equations.

In §5, a two-dimensional TS wave is added to the K-mode flow calculated in §4. Finally, the amplitude of the TS-wave is increased to the point where it is high enough to cause transition.

3. Numerical model

3.1. Governing equations

The governing equations are the incompressible, unsteady Navier–Stokes equations in vorticity–velocity formulation (Fasel, Rist & Konzelmann 1990). They consist of three transport equations for the vorticity components $\omega_x, \omega_y, \omega_z$ in the streamwise (x), normal (y), and spanwise (z) directions, respectively,

$$\frac{\partial \boldsymbol{\omega}}{\partial t} = \nabla \times (\mathbf{u} \times \boldsymbol{\omega}) + \frac{1}{Re} \nabla^2 \boldsymbol{\omega} - \nabla \times \mathcal{F}, \quad (3.1)$$

where \mathcal{F} is a volume force defined in §3.3. Here, the vorticity is defined as the negative curl of the velocity $\boldsymbol{\omega} = -\nabla \times \mathbf{u}$,

$$\omega_x = \frac{\partial v}{\partial z} - \frac{\partial w}{\partial y}, \quad \omega_y = \frac{\partial w}{\partial x} - \frac{\partial u}{\partial z}, \quad \omega_z = \frac{\partial u}{\partial y} - \frac{\partial v}{\partial x}. \quad (3.2)$$

In addition, there are three Poisson equations for the streamwise (u), normal (v), and spanwise (w) velocity components,

$$\frac{\partial^2 u}{\partial x^2} + \frac{\partial^2 u}{\partial z^2} = -\frac{\partial \omega_y}{\partial z} - \frac{\partial^2 v}{\partial x \partial y}, \quad (3.3a)$$

$$\nabla^2 v = \frac{\partial \omega_x}{\partial z} - \frac{\partial \omega_z}{\partial x}, \quad (3.3b)$$

$$\frac{\partial^2 w}{\partial x^2} + \frac{\partial^2 w}{\partial z^2} = \frac{\partial \omega_y}{\partial x} - \frac{\partial^2 v}{\partial y \partial z}. \quad (3.3c)$$

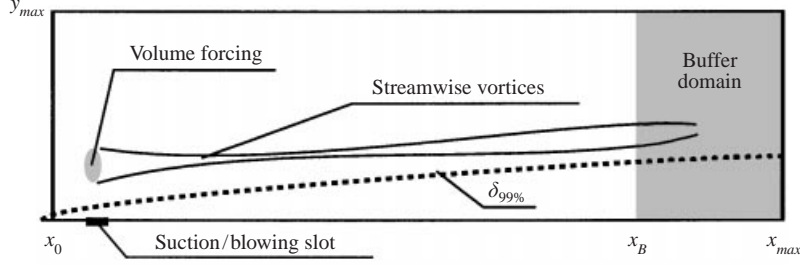


FIGURE 1. Computational domain with volume forcing of free-stream vortices and suction/blowing slot for TS-waves. For better visibility, the y -coordinate is magnified 15 times relative to the x -coordinate.

In these equations, the velocities are normalized by the free-stream velocity U_∞ . The spatial variables x, y, z are normalized by a reference length L , and the time t is normalized by U_∞/L . The global Reynolds number is defined as $Re = U_\infty L/\nu$.

The flow is assumed to be periodic in the spanwise direction z and symmetric with respect to $z = 0$. Therefore, the flow field is expanded in Fourier cosine (u, v, ω_z) and sine (w, ω_x, ω_y) series with K spanwise Fourier modes.

3.2. Boundary conditions

The governing equations are solved inside a rectangular integration domain $x_0 \leq x \leq x_{max}$, $0 \leq y \leq y_{max}$, with periodicity in the spanwise direction z . The computational domain is shown schematically in figure 1.

At the inflow boundary at $x = x_0$, the velocity and vorticity profiles of a steady Blasius boundary layer are specified.

At the wall at $y = 0$ no-slip conditions are imposed on u and w . The normal velocity v is zero over the solid part of the wall and is specified across a narrow suction/blowing slot that is used to generate a two-dimensional TS-wave:

$$v(x, t) = \hat{v} v_s(x) \cos(\omega t) \quad (3.4)$$

where \hat{v} is the amplitude, ω is the angular frequency, and $v_s(x)$ is a shape function that is zero outside the suction/blowing strip and is

$$x_1 \leq x \leq x_c : \quad v_s(\xi) = \frac{1}{48}(729\xi^5 - 1701\xi^4 + 972\xi^3), \quad \xi = \frac{x - x_1}{x_c - x_1}, \quad (3.5a)$$

$$x_c \leq x \leq x_2 : \quad v_s(\xi) = -\frac{1}{48}(729\xi^5 - 1701\xi^4 + 972\xi^3), \quad \xi = \frac{x_2 - x}{x_2 - x_c} \quad (3.5b)$$

within the strip. x_1, x_2 are the beginning and end of the strip, respectively, and $x_c = (x_1 + x_2)/2$ is its centre. Thus, the net volume flow through the strip is zero at any time. This technique has proved to be very effective in generating vorticity disturbance waves with negligible acoustical contents (Fasel *et al.* 1990).

At the free-stream boundary at $y = y_{max}$ the flow is assumed to be irrotational. Thus, all vorticity components and their derivatives are set to zero. A Robin boundary condition is specified for the disturbance velocity v :

$$\left. \frac{\partial v}{\partial y} \right|_{y_{max}} = -\alpha_M v. \quad (3.6)$$

This condition imposes exponential decay $v \propto \exp(-\alpha_M y)$ of disturbances at the free stream. In the case of a TS-wave, this exponential decay follows from linear stability

theory, where α_M is the wavenumber of the TS-wave. For sufficiently large y_{max} the solution is quite insensitive to the value of α_M .

Near the outflow boundary a buffer domain is used to prevent reflections of disturbances. Between $x = x_B$ and $x = x_{max}$, the disturbance vorticity components are gradually ramped down to zero (Kloker, Konzelmann & Fasel 1993). At the outflow boundary, all second derivatives in x are set to zero.

3.3. Generation of free-stream vortices by volume forces

To generate streamwise vortices outside the boundary layer, a (unsteady) volume force $\mathcal{F}(x, y, z, t) = [f_u, f_v, f_w]$ is added to the Navier–Stokes equations. Its components are

$$f_u = \sum_{k=0}^K \widehat{f}_u \exp \left\{ - \left(\frac{x - x f_k}{a f_k} \right)^2 - \left(\frac{y - y f_k}{b f_k} \right)^2 \right\} \cos(\gamma_k z) \cos(\Omega t), \quad (3.7a)$$

$$f_v = \sum_{k=0}^K \widehat{f}_v \exp \left\{ - \left(\frac{x - x f_k}{a f_k} \right)^2 - \left(\frac{y - y f_k}{b f_k} \right)^2 \right\} \cos(\gamma_k z) \cos(\Omega t), \quad (3.7b)$$

$$f_w = \sum_{k=0}^K \widehat{f}_w \exp \left\{ - \left(\frac{x - x f_k}{a f_k} \right)^2 - \left(\frac{y - y f_k}{b f_k} \right)^2 \right\} \sin(\gamma_k z) \cos(\Omega t). \quad (3.7c)$$

Here, $x f_k$, $y f_k$, $a f_k$ and $b f_k$ define the geometry of the forcing of each spanwise Fourier mode, \widehat{f}_u , \widehat{f}_v and \widehat{f}_w are the amplitudes, and Ω is the frequency. By trial and error, these parameters were adjusted such that the characteristics of the numerically generated K-mode matched those of the experimental observations.

In the calculations, the curl $\nabla \times \mathcal{F}$ is used as a source term on the right-hand side of the vorticity transport equations.

3.4. Numerical method

The streamwise and wall-normal derivatives are discretized with compact differences, and the spanwise derivatives are treated pseudospectrally. A semi-implicit combination of a three-stage Runge–Kutta and a Crank–Nicolson method is used for the time integration. A detailed description of the numerical method is given by Meitz (1996).

In each of the case studies in the present paper, several test calculations were performed to establish appropriate values of the relevant numerical parameters. In each case, the spatial and temporal discretization, the size of the integration domain, and the boundary conditions were adjusted until further refinement did not change the relevant solution parameters (e.g. the amplitudes of the dominant disturbance components) by more than 2%. The parameters used in the calculations are listed in table 1.

4. Numerical model of the K-mode

4.1. Linear evolution of spanwise perturbations

For the calculations in this section, the Navier–Stokes equations were linearized about the Blasius boundary layer flow. Available experimental data provide a range of spanwise wavenumbers and frequencies to consider for the numerical simulation: Kendall (1985) measured a typical spanwise spacing between streaks (i.e. a spanwise wavelength) of 12 local Blasius displacement thicknesses δ at a Reynolds number $Re_\delta = 1740$, which corresponds to a spanwise wavenumber $\gamma = 30$ in the present

$U_\infty = 15 \text{ m s}^{-1}$,	$L = 0.1 \text{ m}$	$\nu = 15 \times 10^{-6} \text{ m}^2 \text{ s}^{-1}$	
$x_0 = 0.1$ ($Re_\delta = 172$),	$x_B = 6.55$,	$x_{max} = 8.1$ ($Re_\delta = 1549$),	801 gridpoints in x -direction
$y_{max} = 0.15$ ($= 87\delta_0$),	$\alpha_M = 28$,	$\Delta y_{wall} = 0.1786 \times 10^{-3}$,	80 gridpoints in y -direction
$\Delta t = 7.854 \times 10^{-3}$			
Free-stream vortices generated by volume forces with parameters			
$xf_k = 0.5$,	$yf_k = 0.04$,	$af_k = 3.3 \times 10^{-2}$,	$bf_k = 5 \times 10^{-3}$, $\widehat{fu}_k = 0$, $\widehat{fv}_k = 0$
case LIN-0:	$F = 0$,	$\gamma = 30k$, for $k = 1, \dots, 4$,	$\widehat{fw}_k = 0.1$
case LIN-0.1:	$F = 0.1$,	$\gamma = 30k$, for $k = 1, \dots, 4$,	$\widehat{fw}_k = 0.1$
case NL-weak:	$F = 0.1$,	$\gamma = 30k$, for $k = 1, \dots, 4$,	$\widehat{fw}_k = 0.1$, for $k = 1, 2, 3, 4$
case NL-1:	$F = 0.1$,	$\gamma = 60k$, for $k = 2, 4, \dots, 38, 40$	$\widehat{fw}_2 = 1$
case NL-mult:	$F = 0.1$,	$\gamma = 30k$, for $k = 1, \dots, 20$	$\widehat{fw}_2 = 1$, $\widehat{fw}_k = 0.1$, for $k = 1, 3, 4$

TABLE 1. Computational parameters for K-mode calculations.

non-dimensional units. Westin *et al.* (1994) found a spanwise wavelength of 7δ at $Re_\delta = 890$ and of 5.5δ at $Re_\delta = 1260$, corresponding to $\gamma = 100$ and $\gamma = 90$, respectively. They also found that the energy density spectrum inside the boundary layer, at $Re_\delta = 890$, was nearly flat for frequencies up to $F = 0.1$ and dropped off for higher frequencies. Here, $F = 2\pi f^* \nu / U_\infty^2 \times 10^4$, where f^* is the frequency in Hz.

With this in mind, calculations were performed for four spanwise wavenumbers ranging from $\gamma = 30$ to $\gamma = 120$, and for two frequencies: $F = 0$, i.e. steady perturbations, and $F = 0.1$. These calculations will be referred to as case ‘LIN’. The u -amplitudes of the disturbances inside the boundary layer are plotted in figure 2(a) for steady disturbances (case LIN-0) and in figure 2(b) for unsteady disturbances (case LIN-0.1). Except for the spanwise mode $k = 1$ (i.e. $\gamma = 30$) in the unsteady case LIN-0.1, all disturbance amplitudes grow in x . In both cases, disturbances with a spanwise wavenumber $\gamma = 60$, i.e. spanwise mode $k = 2$, have the highest amplitudes. This agrees well with the experimental observations cited above. A comparison between the two figures shows that the amplitude of steady disturbances is generally higher than those of unsteady fluctuations with the same spanwise wavenumber.

In figure 3, the amplitude profiles of the spanwise modes $k = 2$ are plotted vs. the normal coordinate y , at the streamwise location $x = 3.7$. In these plots, all amplitude curves are normalized by the u -amplitude of the steady mode $k = 2$, since that mode has the highest amplitude at that x location. Thus, the amplitude profile $u_{amp}(y, F = 0, k = 2)$ has a maximum of 1. In addition, the Blasius profiles u_B, v_B, ω_{zB} are plotted for comparison. The y -coordinate is normalized by the local Blasius displacement thickness δ .

The free-stream vortices can be clearly discerned in the plots of the normal and transverse velocities v and w and the streamwise vorticity ω_x . The centre of the vortices, at $y/\delta = 4.5$, is marked by a local maximum of the w -amplitude. Inside the boundary layer ($y/\delta \leq 3$) the fluctuations are dominated by the streamwise velocity component u and by its contribution to the normal and spanwise vorticity components. The streamwise vorticity component ω_x , which does not contain any derivative of u , is two orders of magnitude smaller than ω_y and ω_z inside the boundary layer, and is also substantially smaller there than in the free-stream vortices. These observations suggest that the boundary layer response to free-stream turbulence is primarily a spanwise modulation of the streamwise velocity. Thus, the streaks seen in experimental flow visualizations are not due to strong streamwise vortices but are

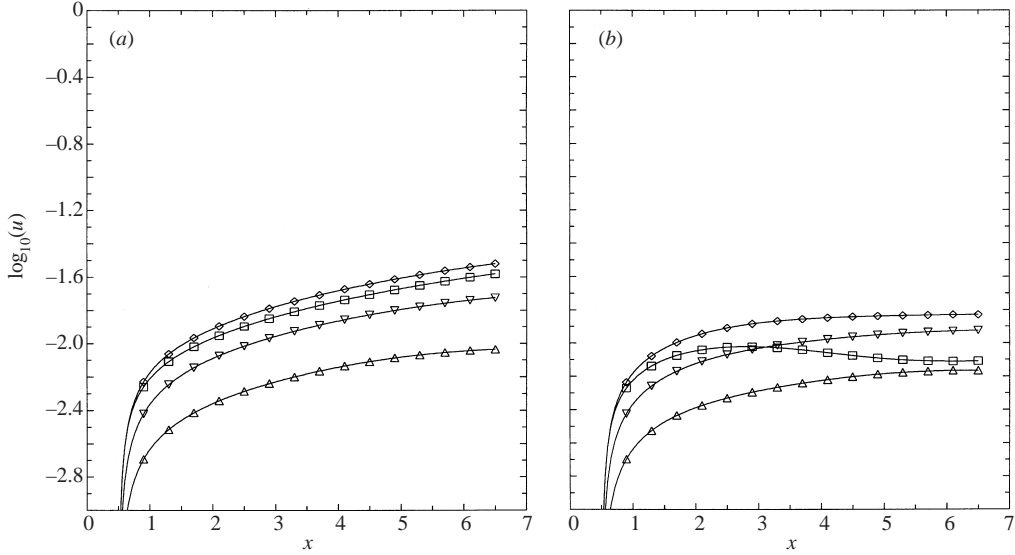


FIGURE 2. Case LIN: amplitudes of (a) steady disturbances and (b) disturbances with frequency $F = 0.1$, and spanwise wavenumber $\gamma = 30k$. The curves are for $k = 1$ (\square), $k = 2$ (\diamond), $k = 3$ (∇), $k = 4$ (\triangle).

mere artifacts of this spanwise modulation. Such an interpretation of the K-mode agrees with the experimental observations by Klebanoff (1971), who describes it as ‘a periodic thickening/thinning of the boundary layer’.

Further insight into the nature of the boundary layer perturbations can be gained from the amplitude scaling in x and y . In figures 4(a) and 4(b), the ratios of the u -amplitudes $A(x)/A(x = 0.5)$ are plotted. The amplitudes of the steady disturbances are seen to scale as $x^{3/4}$, whereas the amplitudes of the unsteady disturbances do not scale with any power of x . While the streamwise growth of the steady perturbations is higher than observed in the experiments ($\propto x^{1/2}$), the streamwise growth of the unsteady disturbances with frequency $F = 0.1$ is lower. Hence, one can expect that it is possible to find a suitable combination of frequencies between $F = 0$ and $F = 0.1$ such that the average (i.e. r.m.s.) amplitudes exhibit the proper scaling in x .

The u -amplitude profiles of the steady disturbance modes $k = 1, 2$ are nearly self-similar when plotted vs. the Blasius similarity variable

$$\eta = \frac{y}{\sqrt{Re_x}} \left[= 1.72 \frac{y}{\delta} \right]. \quad (4.1)$$

In fact, a good approximation of the Navier–Stokes results is found by inspection as

$$u(x, y, z) = C_{FST} x^{3/4} (f' - \frac{1}{3} \eta f'') f'' \cos(\gamma z) \quad (4.2)$$

where C_{FST} is a receptivity coefficient and $f(\eta)$ is the solution of the Blasius equation

$$f f'' + 2 f''' = 0. \quad (4.3)$$

This function is plotted in figure 5. The Navier–Stokes results, scaled by $x^{3/4}$, are plotted for comparison. The steady disturbance modes $k = 1, 2$ scale remarkably well with this normalization. Except for the first streamwise location $x = 1.3$, the amplitude profiles neatly collapse into one curve. The above scaling does not work quite as well for the steady disturbance modes $k = 3, 4$. The unsteady disturbances

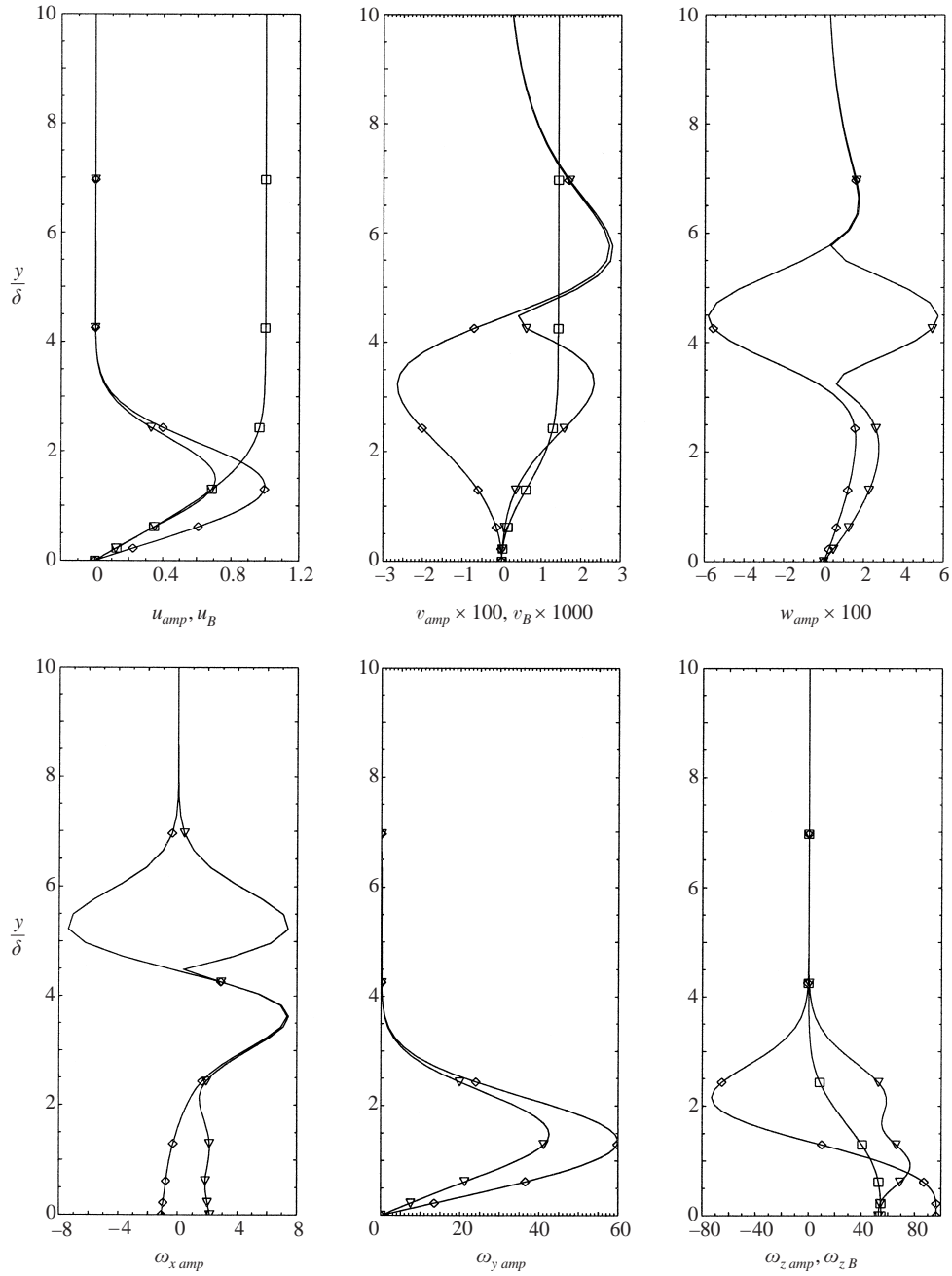


FIGURE 3. Case LIN: amplitude profiles vs. y/δ at $x = 3.7$. The curves are: \square , Blasius profile; \diamond , amplitude of steady disturbances with spanwise wavenumber $\gamma = 60$; ∇ , amplitude of unsteady disturbances with spanwise wavenumber $\gamma = 60$ and frequency $F = 0.1$. All amplitude curves (\diamond , ∇) are normalized with the maximum value of u_{amp} ($F = 0$, $\gamma = 60$).

do not fit this scaling. It is certainly noteworthy that the most amplified modes are those whose amplitude profiles are self-similar.

To get a better understanding of the evolution of the unsteady disturbances, the phase velocity c is plotted in figure 6. Outside the boundary layer, at $y = 0.106$, $c \approx 1$.

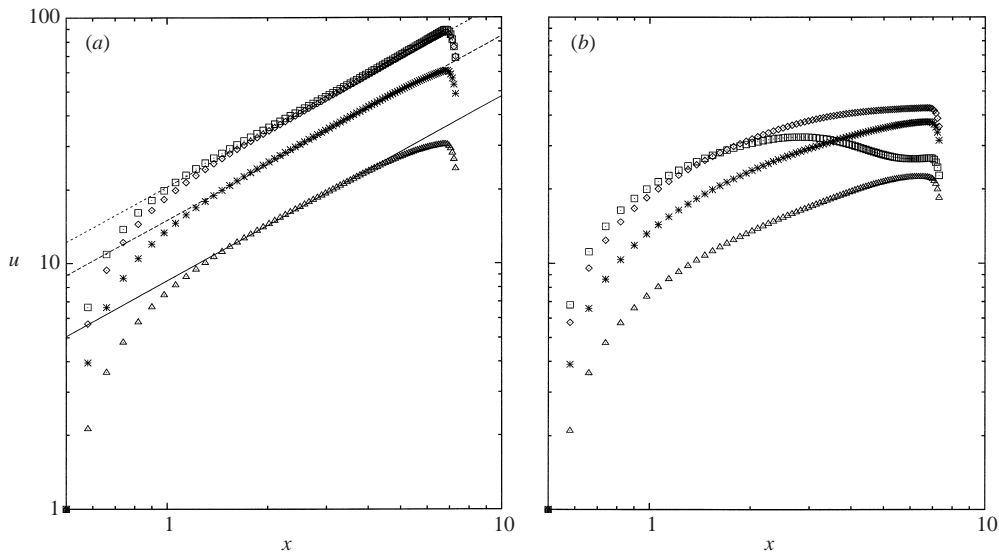


FIGURE 4. Case LIN: ratio of the u -amplitudes $A(x)/A(x = 0.5)$ of (a) steady disturbances and (b) disturbances with frequency $F = 0.1$, with spanwise wavenumber $\gamma = 30k$. The curves are for $k = 1$ (\square), $k = 2$ (\diamond), $k = 3$ ($*$), $k = 4$ (\triangle). The straight lines in (a) are $\propto x^{0.75}$.

Near the wall, c varies considerably, increasing from $c = 0.55$ for mode $k = 1$ near the upstream end of the integration domain at $x = 0.1$ to $c = 1.05$ at $x = 5$. Except for mode $k = 1$, the values of c are lowest near the amplitude maxima in y_{Amax} . A detailed investigation of the phase velocity shows that $c(x, y = y_{Amax})$ is considerably less than the velocity of the Blasius boundary layer at those locations. Due to the increase of c with y , the phases inside the boundary lag those outside, hence the phase curves are bent toward the wall. This could explain Kendall's observation that 'disturbances appear to move toward the wall'.

4.2. Weakly nonlinear evolution of spanwise perturbations

In this section, the development of low-amplitude disturbances is investigated using the full, nonlinear Navier–Stokes equations. Since the ultimate goal is to model the effects of free-stream turbulence, only unsteady perturbations with frequency $F = 0.1$ were considered. Also, to allow for the nonlinear generation of higher spanwise wavenumbers, $K = 20$ spanwise Fourier modes were used in this calculation; however, only the first four $k = 1, \dots, 4$ were forced. The first spanwise Fourier mode $k = 1$ had a spanwise wavenumber $\gamma = 30$, corresponding to $\lambda_z = 0.20944$. All other computational parameters were the same as in the linear calculation in §4.1. This allows for a direct comparison with the linear calculations, and thus for an assessment of nonlinear effects. This simulation will be referred to as case 'NL-weak'.

The u -amplitudes of the disturbances inside the boundary layer are plotted in figure 7. The curves for disturbances with frequency $F = 0.1$ are virtually identical to those in figure 2(b). Since disturbances with other frequencies are not generated by direct forcing but through nonlinear interactions, their amplitudes are much smaller than those of the forced disturbances with $F = 0.1$. These curves indicate that, with the low amplitudes used in this simulation, nonlinear effects are negligible in the development of the forced modes. The r.m.s.-amplitude of the u -disturbance, averaged over t and z , is plotted in figure 8. The maximum r.m.s.-amplitude is less than 2% of

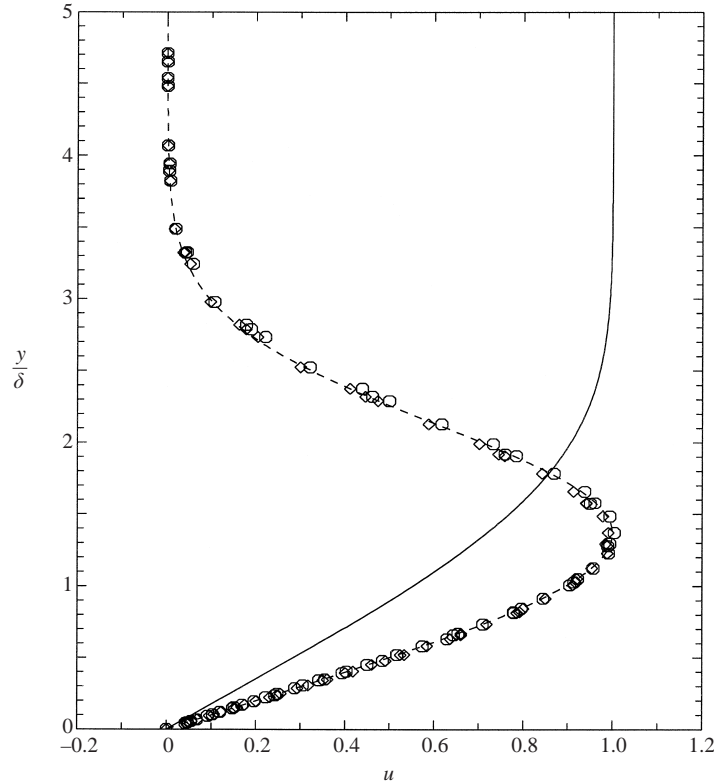


FIGURE 5. Case LIN-0: amplitude profiles of steady disturbances $u(x, y)$, plotted vs. the normal coordinate y scaled by the local displacement thickness $\delta(x)$. The curves are: \diamond , Navier–Stokes, $k = 1$, at $x = 1.1, 2.5, 3.7, 4.9$, scaled by $x^{3/4}$; \circ , Navier–Stokes, $k = 2$, at $x = 1.1, 2.5, 3.7, 4.9$, scaled by $x^{3/4}$; ---, similarity function $x^{3/4}(f' - \eta/3f'')f''$; —, Blasius velocity $u_n \equiv f'$.

U_∞ . This is a low value compared to K-mode r.m.s.-amplitudes in experiments, which can be as high as 15%. Note that the r.m.s.-amplitude does not scale with any power of x . In addition, there is no self-similarity in the $u_{rms}(y)$ profiles (not shown here).

Time signals $u(t)$ are plotted in figure 9. The curves show the evolution of u in time at several x locations, in the centreplane $z = 0$, at the respective y location of maximum amplitude. Note the deformation of the curves for increasing x . While the signal at $x = 1.3$ is almost identical to that of a pure sine-wave, that at $x = 6.1$ is somewhat reminiscent of a sawtooth wave. This shape change is not due to nonlinear effects, since these were shown earlier to be negligible. Rather, it is due to the different phase velocities of the individual spanwise Fourier modes. Recall from figure 6 that higher spanwise Fourier modes have a slightly higher phase velocity. Thus, the different modes combine to form a travelling bump with a maximum in the plane $z = 0$.

4.3. Single wavenumber excitation of the K-mode

In this section, the nonlinear response of a Blasius boundary layer to a high-amplitude free-stream disturbance wave with frequency $F = 0.1$ and spanwise wavenumber $\gamma = 60$, corresponding to $\lambda_z = 0.10472$, is calculated. The wavenumber $\gamma = 60$ was chosen because the linear (and weakly nonlinear) response of the boundary layer is strongest at this wavenumber, as shown in the previous sections. Again, the full

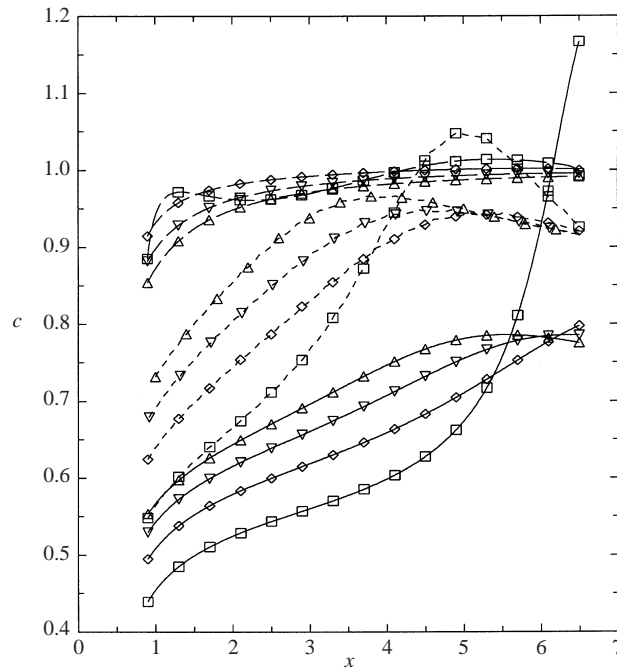


FIGURE 6. Case LIN: phase velocity of disturbances with frequency $F = 0.1$ and spanwise wavenumber $\gamma = 30k$. The curves are for $k = 1$ (\square), $k = 2$ (\diamond), $k = 3$ (∇), $k = 4$ (\triangle), at three different distances from the wall: outside the boundary layer at $y = 0.106$ (---), near the wall at $y = 7.8 \times 10^{-4}$ (-.-.-), and at the y location of maximum amplitude (—).

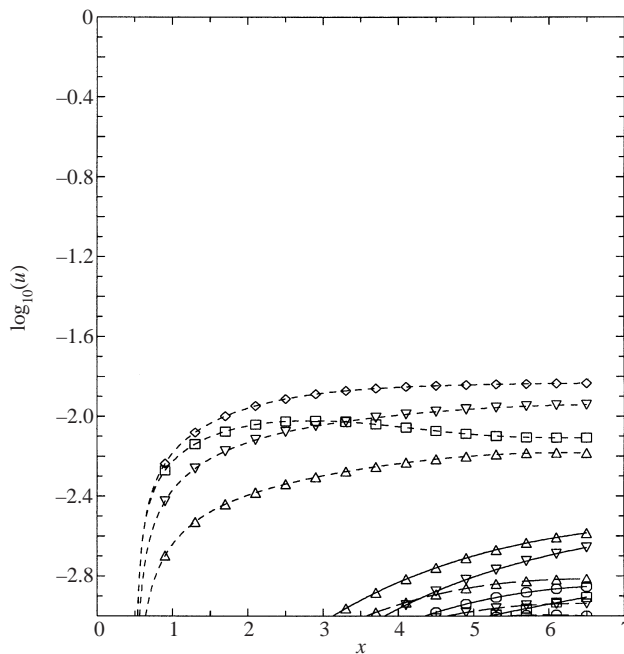
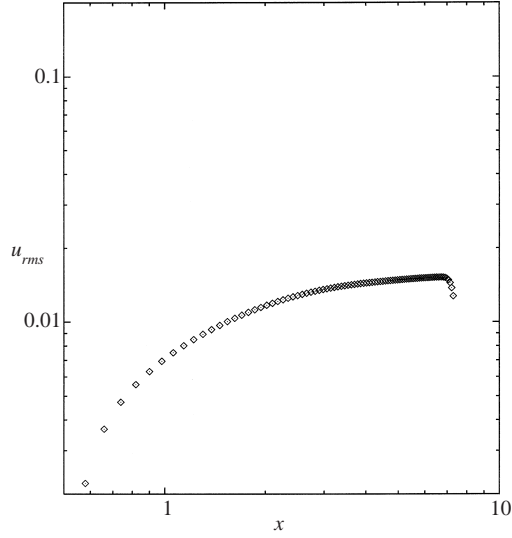
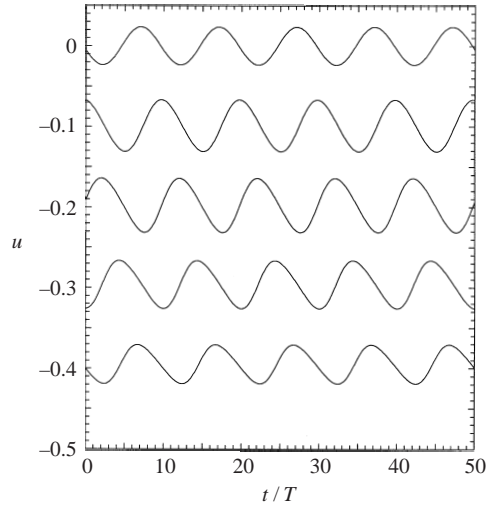


FIGURE 7. Case NL-weak: amplitudes of disturbances with frequencies $F = 0$ (—), $F = 0.1$ (---), and $F = 0.2$ (-.-.-) and spanwise wavenumber $\gamma = 30k$. The curves are for $k = 1$ (\square), $k = 2$ (\diamond), $k = 3$ (∇), $k = 4$ (\triangle).

FIGURE 8. Case NL-weak: root-mean-square disturbance $u_{rms}(x)$.FIGURE 9. Case NL-weak: u plotted vs. t/T , for several streamwise locations x , in the plane $z = 0$. Each curve is taken at the respective y location of maximum amplitude. Top curve at $x = 1.3$, bottom curve at $x = 6.1$, x -increment between consecutive curves is 1.2. The vertical offset between consecutive curves corresponds to $u = 0.1$.

nonlinear Navier–Stokes equations were used, with 20 spanwise Fourier modes. Since there was no forcing of disturbance components with a spanwise wavenumber $\gamma = 30$, the lowest spanwise wavenumber in this calculation was chosen as $\gamma = 60$. For the sake of consistent labelling of modes, this Fourier mode will be referred to as $k = 2$. Thus, the calculation was carried out with spanwise Fourier modes $k = 0, 2, 4, 6, \dots, 38, 40$, corresponding to spanwise wavenumbers $\gamma = 0, 60, 120, \dots, 1200$. Only the spanwise Fourier mode $k = 2$ was forced, with a forcing amplitude $\widehat{fw}_k = 1$. All other computational parameters were the same as in the linear calculation in §4.1. This calculation will be referred to as case ‘NL-1’.

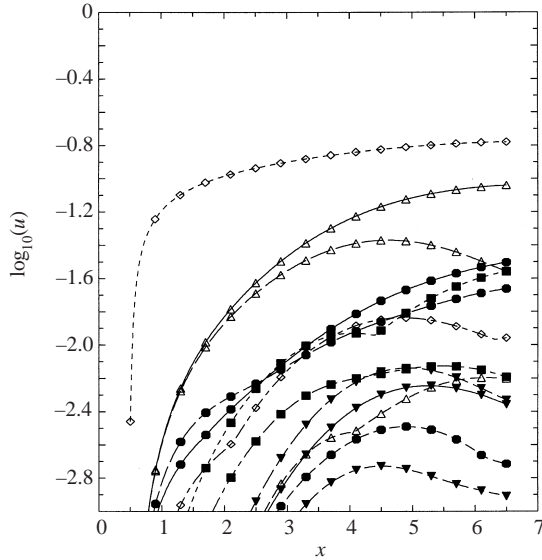


FIGURE 10. Case NL-1: amplitudes of disturbances with frequencies $F = 0$ (—), $F = 0.1$ (---), $F = 0.2$ (---), and $F = 0.3$ (—) and spanwise wavenumber $\gamma = 30k$. The curves are for $k = 0$ (●), $k = 2$ (◇), $k = 4$ (△), $k = 6$ (■), $k = 8$ (▼).

The u -amplitudes of the disturbances inside the boundary layer are plotted in figure 10. Due to the higher forcing amplitude, the curve for $F = 0.1$, $k = 2$ is shifted up by one unit on the logarithmic ordinate axis relative to the curve $F = 0.1$, $k = 2$ in figure 7. A close inspection also reveals that its shape is slightly different: initially, the amplitude in figure 10 is lower than expected, but then it grows more strongly in x than the corresponding curve in figure 7. This change of the growth rate is clearly a nonlinear effect. The much higher amplitude level also causes the nonlinear generation of numerous other modes. The nonlinear modes with the highest amplitudes are mode $F = 0$, $k = 4$ and mode $F = 0.2$, $k = 2$. Note that the shape of the amplitude curves of the steady mode $F = 0$, $k = 4$ is substantially different from that of the linear calculation in figure 2(b).

The r.m.s.-amplitude of the u -disturbance, averaged over t and z , is plotted in figure 11. The maximum r.m.s.-amplitude is higher than 10% of U_∞ , which is on the order of the r.m.s.-amplitude levels measured in experiments. Equally important is the fact that the r.m.s.-amplitude curve scales as $x^{0.6}$, which is only slightly higher than the \sqrt{x} scaling observed in experiments. Also, in contrast to the case NL-weak, the r.m.s.-amplitudes are nearly self-similar. The development of the r.m.s.-amplitude profiles can again be expressed in terms of the Blasius function $f(\eta)$:

$$u_{rms}(x, y) = C_{FST} x^{0.6} (f' - \frac{1}{5} \eta f'') f'' \quad (4.4)$$

This scaling function is slightly different from that in equation (4.2), indicating a shift of the maximum toward the wall. In figure 12, the similarity function is plotted, along with the results from the Navier–Stokes calculation and experimental data. There is reasonable agreement between the data from Westin *et al.* (1994) at $Re_\delta = 890$, the data from Kendall (1985) at $Re_\delta = 1233$, and the Navier–Stokes results in the inner part of the boundary layer, up to the maximum r.m.s.-amplitude at $y/\delta = 1.3$. In the outer part of the boundary layer, the experimental r.m.s. values, particularly the ones from Boiko *et al.* (1994), are higher than the numerical values, and they

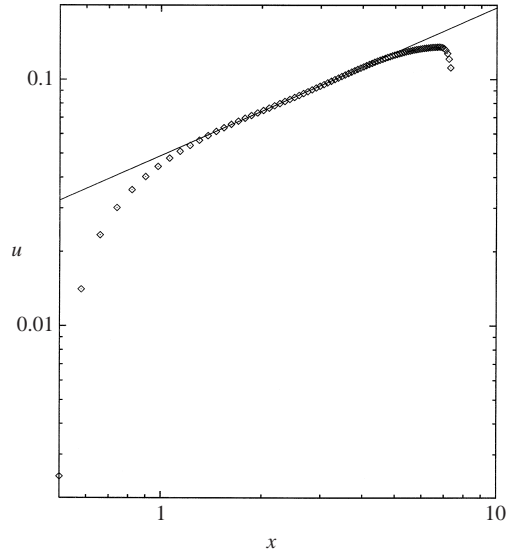


FIGURE 11. Case NL-1: root-mean-square disturbance $u_{rms}(x)$. The straight line is $\propto x^{0.6}$.

approach a higher value at the free stream. The discrepancy near the free stream is almost certainly due to the different origin of the free-stream perturbations. In the experiments, free-stream turbulence was generated by placing grids into the flow, which, at low frequencies, mainly excited longitudinal (u) fluctuations (Westin *et al.* 1994). In the numerical simulations, the free-stream vortices were generated by volume forces in the spanwise direction, exciting primarily w -fluctuations.

Time signals $u(t)$ are plotted in figure 13. The curves show the evolution of u in time at several x locations, in the centreplane $z = 0$, at the respective y location of maximum amplitude. The time t on the abscissa is scaled by T , where $10 T$ is the period corresponding to the frequency $F = 0.1$ of the K-mode. The change of the signal from a sine wave at $x = 1.3$ to a sawtooth wave further downstream is more pronounced than in figure 9, underlining the important role of nonlinearity in this flow.

Instantaneous K-mode velocity profiles $u(y, z)$ are plotted in figure 14. These plots illustrate the change of the velocity profile associated with the thickening–thinning of the boundary layer in the spanwise direction and in time.

A more detailed view of the velocity profiles is given in figure 15. Here, the total flow $u_T = u_{Kleb} + u_B$ at $x = 4.9$ is plotted vs. y/δ , at different times t and at spanwise locations $z = 0$, $z = \lambda_z/4$, and $z = \lambda_z/2$. In addition to the thickening–thinning of the boundary layer, these curves also show another distinct characteristic: the profiles at $(z = 0, t/T = 1)$, $(z = 0, t/T = 3.5)$, and $(z = 0.02618, t/T = 3.5)$ are inflectional. This has important consequences for the stability of the flow, which will be discussed later.

Overall, the agreement between the numerical simulation and the experimental data is surprisingly good. The forcing of a single disturbance component outside the boundary layer is sufficient to produce a disturbance flow inside the boundary layer whose key characteristics match those of the K-mode measured in experiments with a broad spectrum of free-stream disturbances. A crucial observation is that the high-amplitude disturbances cause nonlinear effects that qualitatively change the

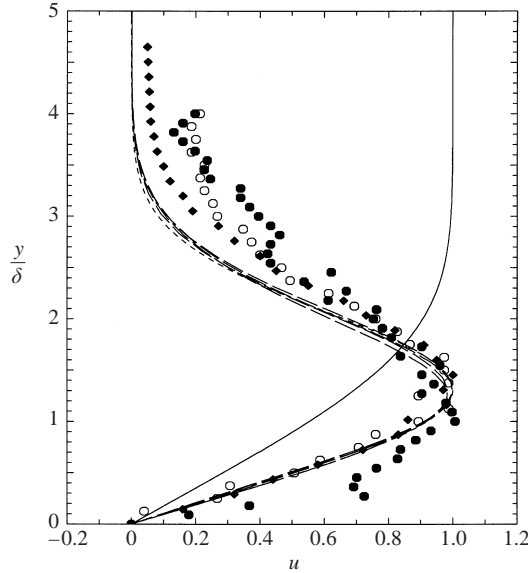


FIGURE 12. Case NL-1: amplitude profiles of root-mean-square disturbances $u_{rms}(x, y)$, plotted vs. the normal coordinate y scaled by the local displacement thickness $\delta(x)$. The curves are: $-\cdot-$, Navier–Stokes at $x = 1.1, 2.5, 3.7, 4.9$, scaled by $x^{0.6}$; $----$, similarity function $x^{0.6}(f' - \eta/5f'')f''$; $—$, Blasius velocity $u_B \equiv f'$; \blacklozenge , experimental data $Re_\delta = 1233$ from Kendall (1985); \circ , experimental data at $Re_\delta = 890$ from Westin *et al.* (1994); \bullet , experimental data at $Re_\delta = 1260$ from Westin *et al.* (1994).

scaling of the disturbances in both x and y . This suggests that approaches based on a linear perturbation of the Blasius boundary layer are intrinsically unsuitable for a quantitative modelling of the K-mode.

4.4. Multiple wavenumber excitation of the K-mode

The parameters for this simulation were similar to those of the previous simulation in §4.3: mode $F = 0.1, k = 2$ was forced with a high amplitude $\widehat{fw}_k = 1$. In addition, however, modes $F = 0.1, k = 1, 3, 4$ were also forced, with the low amplitude $\widehat{fw}_k = 0.1$. $K = 20$ spanwise Fourier modes were used, the lowest spanwise mode being $k = 1$ with $\gamma = 30$. All other computational parameters were the same as in the linear calculation in §4.1. This simulation will be referred to as case ‘NL-mult’.

The u -amplitudes of the disturbances with frequencies $F = 0, \dots, 0.3$ inside the boundary layer are plotted in figures 16(a)–16(d). Disturbances with higher frequencies were present, but with very small amplitudes. The highest amplitude curves (with amplitudes $> 10^{-2}$) are virtually identical to those in figure 10. However, the presence of the additional three forced modes leads to the nonlinear generation of several other modes that were not present (or very small) in figure 10, most notably modes with $k = 1$. The growth of the high-amplitude mode $F = 0.1, k = 2$ is identical to the one in figure 10 from §4.3 and close to those in §§4.1 and 4.2.

The evolution of the forced modes with small forcing amplitude ($F = 0.1, k = 1, 3, 4$) in figure 16(b) is quite different from that in the linear and low-amplitude calculations in §§4.1 and 4.2. This indicates that the nonlinear interaction with mode $F = 0.1, k = 2$ is more important than the linear behaviour intrinsic to those modes. However, mode $F = 0.1, k = 2$ is by far the dominant disturbance component of the flow (see

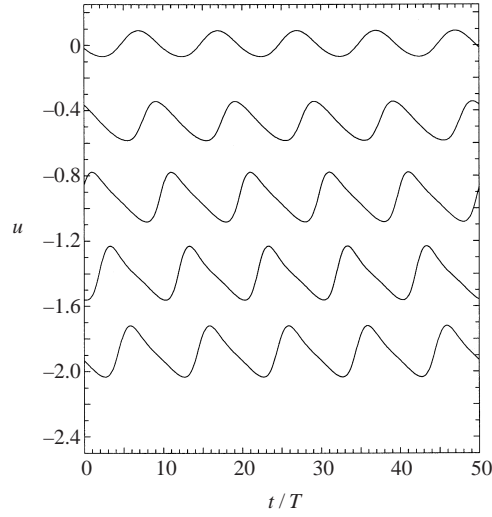


FIGURE 13. Case NL-1: u plotted vs. t/T , for several streamwise locations x , in the plane $z = 0$. Each curve is taken at the respective y location of maximum amplitude. Top curve at $x = 1.3$, bottom curve at $x = 6.1$, x -increment between consecutive curves is 1.2. The vertical offset between consecutive curves corresponds to $u = 0.5$.

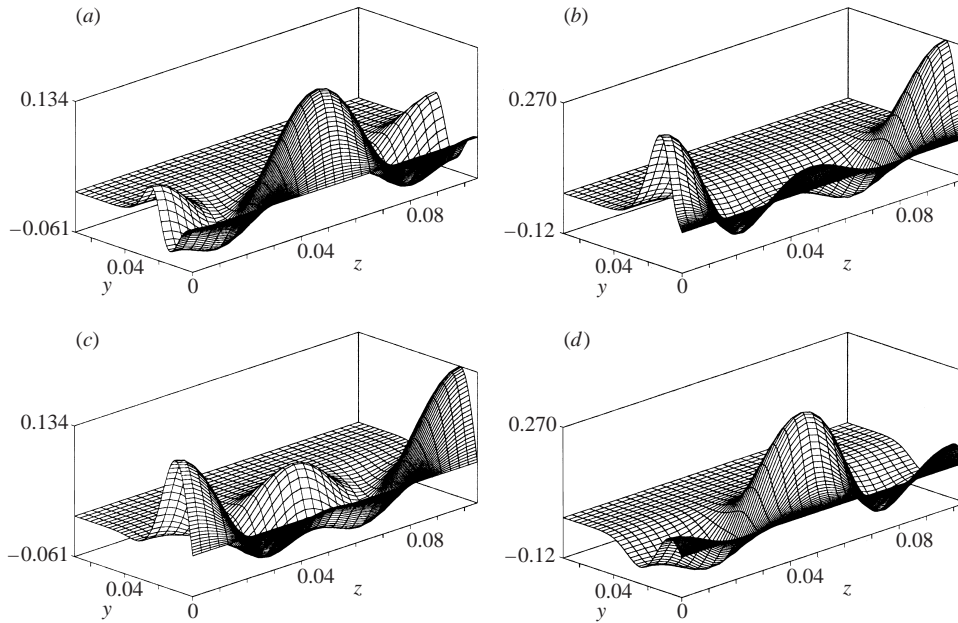


FIGURE 14. Case NL-1: disturbance velocity u plotted over (y, z) at $x = 4.9$ and at $t/T = 1$ (a), $t/T = 3.5$ (b), $t/T = 6$ (c) and $t/T = 8.5$ (d).

figure 16(b). Hence, the time signals $u(t)$ and the evolution of the r.m.s.-amplitudes in x and y are almost the same as in §4.3. Thus, they are not plotted here.

Overall, the low-amplitude forcing of the additional spanwise modes does not appear to have a significant impact on the characteristics of the ‘numerical K-mode’, compared to the single mode forcing in §4.3.

Suction/blowing slot between $x = 0.48$ ($Re_\delta = 377$) and $x = 0.72$ ($Re_\delta = 462$), $F = 1$,
Case TS-NL-1: $\hat{v} = 1 \times 10^{-3}$
Case TS-NL-mult: $\hat{v} = 1 \times 10^{-3}$
Case TS-trans: $\hat{v} = 2 \times 10^{-3}$

TABLE 2. Computational parameters for generation of TS-waves.

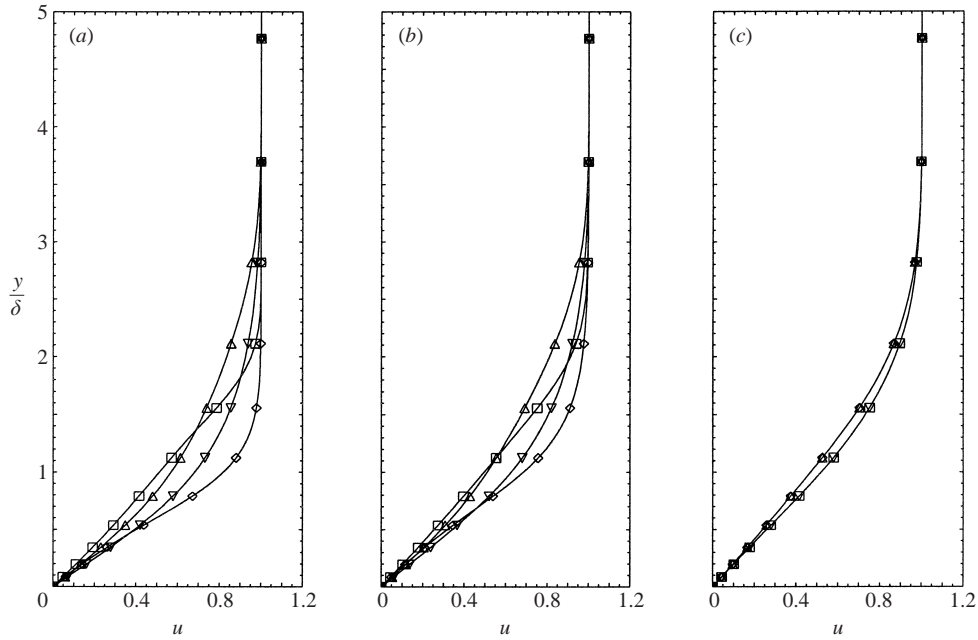


FIGURE 15. Case NL-1: profiles of the total velocity u_T at $x = 4.9$ and at $z = 0$ (a), $z = 0.02618$ (b), and $z = 0.05234$ (c), plotted vs. the normal coordinate y scaled by the local Blasius displacement thickness $\delta(x)$. The curves are: \square , $t/T = 1$; \diamond , $t/T = 3.5$; ∇ , $t/T = 6$; \triangle , $t/T = 8.5$.

5. Interaction of the K-mode with a Tollmien–Schlichting wave

From experiments and from the calculations in the previous section it is apparent that the K-mode does not directly cause transition, at least not for disturbance amplitude levels $u_{rms} < 15\% U_\infty$. Thus, there must be some instability mechanism, which may be affected by, but is distinct from, the K-mode, that causes transition. Experimental evidence (Kendall 1992) suggests that TS-waves may play a crucial role in transition even in the presence of the K-mode.

In the present numerical investigation, the interaction between the K-mode and TS-waves is studied by introducing a two-dimensional TS-wave into the unsteady boundary layer flows computed in §§4.3 and 4.4. A suction/blowing slot near the inflow boundary is used to generate the TS-wave. The frequency $F = 1$ of the TS wave is chosen such that it is ten times the frequency $F = 0.1$ of the free-stream vortices that excite the K-mode. Hence, $T = 1$ is the period of the TS-wave. The parameters used for the generation of the TS-wave are listed in table 2.

In §5.1, a two-dimensional TS wave is added to the single-wavenumber, high-amplitude K-mode flow calculated from case NL-1 in §4.3. In §5.2, a TS-wave is added to the multiple wavenumber flow from case NL-mult in §4.4. Finally, using

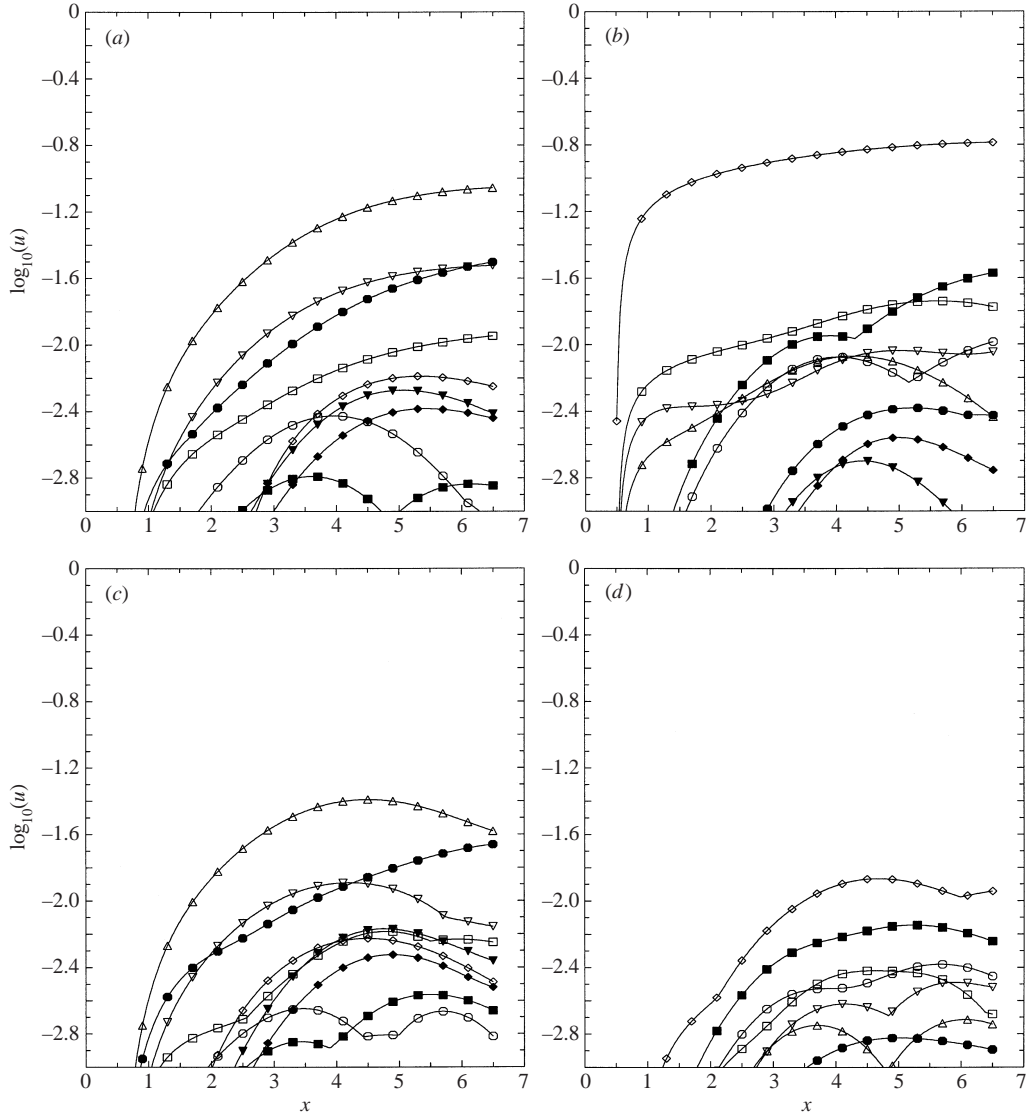


FIGURE 16. Case NL-mult: amplitudes of disturbances with spanwise wavenumber $\gamma = 30k$. The curves are for $k = 0$ (\bullet), $k = 1$ (\square), $k = 2$ (\diamond), $k = 3$ (∇), $k = 4$ (\triangle), $k = 5$ (\circ), $k = 6$ (\blacksquare), $k = 7$ (\blacklozenge), $k = 8$ (\blacktriangledown). (a) Steady disturbances, (b) $F = 0.1$, (c) $F = 0.2$, (d) $F = 0.3$.

the K-mode flow from §4.4, the amplitude of the TS-wave is increased to the point where it is sufficiently high to cause transition.

5.1. Single-wavenumber excitation of the K-mode

In this section, a two-dimensional TS wave is added to the K-mode flow from case NL-1 in §4.3. Hence, this calculation will be referred to as case ‘TS-NL-1’. To better analyse the results of this simulation, the K-mode flow computed in §4.3 was subtracted from the flow computed here. This decomposition allowed a separation of the TS-disturbances (i.e. the original TS-wave and any waves due to nonlinear interaction) from the K-mode.

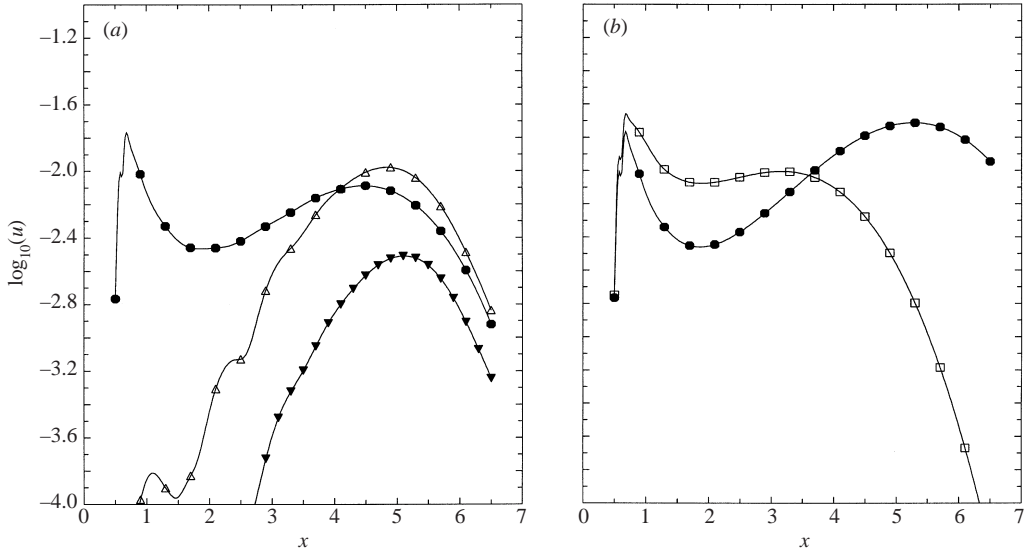


FIGURE 17. (a) Case TS-NL-1: amplitudes of TS-disturbances with frequency $F = 1$ and spanwise wavenumber $\gamma = 30k$. The curves are for $k = 0$ (\bullet), $k = 4$ (\triangle), $k = 8$ (\blacktriangledown). (b) As (a) but linear reference calculation without Klebanoff-mode. The curves are for $k = 0$ (\bullet) (two-dimensional wave), $k = 1$ (\square) (three-dimensional wave).

In figure 17(a), the amplitudes of disturbance waves with frequency $F = 1$ and spanwise wavenumbers $\gamma = 30k$ are plotted. Apart from the two-dimensional TS-wave with spanwise wavenumber 0, only waves with spanwise indices $k = 4, 8$ have significant amplitudes. These waves are due to nonlinear interactions between the two-dimensional TS wave and the steady components $F = 0$, $k = 4, 8$ of the K-mode. Indeed, the steady modes with the highest amplitudes in figure 10 are those with $k = 4, 0$, and 8. For comparison, the amplitudes of TS-waves obtained from a linear reference calculation, without the K-mode, are plotted in figure 17(b). In the reference calculation, only TS-waves with spanwise wavenumbers $\gamma = 0$ (two-dimensional) and $\gamma = 30$ (i.e. $k = 1$) are amplified; all higher spanwise modes are damped. A noteworthy aspect of these plots is the fact that the highest amplitude is not attained by the two-dimensional TS-wave with $k = 0$, but by the disturbance wave with $k = 4$. Equally important, the two-dimensional TS-wave is less amplified than that in the linear calculation in figure 17(b). This reduced amplification agrees qualitatively with the measurements by Boiko *et al.* (1994).

The amplitude curves in figure 10 suggest that other important nonlinear interactions would involve the two-dimensional TS-wave and modes $F = 0.1$, $k = 2, 6$ to generate modes $F = 0.9, 1.1$, $k = 2, 6$ and mode $F = 0.2$, $k = 4, 0$, to generate modes $F = 0.8, 1.2$, $k = 0, 4, 8$. The amplitudes of disturbance waves with frequencies $F = 0.9$ and $F = 1.1$ are plotted in figure 18(a). Only waves with spanwise indices $k = 2$ and $k = 6$ have significant amplitudes, just as expected from the amplitudes in figure 10. Figure 18(b) shows the amplitude curves of TS-disturbances with frequencies $F = 0.8$ and $F = 1.2$, with the dominant modes $k = 0, 4, 8$, again as expected.

The phase velocities of TS-disturbances with frequency $F = 1$ are plotted in figure 19(a). The large fluctuations of the curves for the three-dimensional waves are due to the fact that the amplitudes of these waves are very small for $x < 2.5$ ($k = 4$) and $x < 3.5$ ($k = 8$), see figure 17(a). At such small amplitudes the calculation

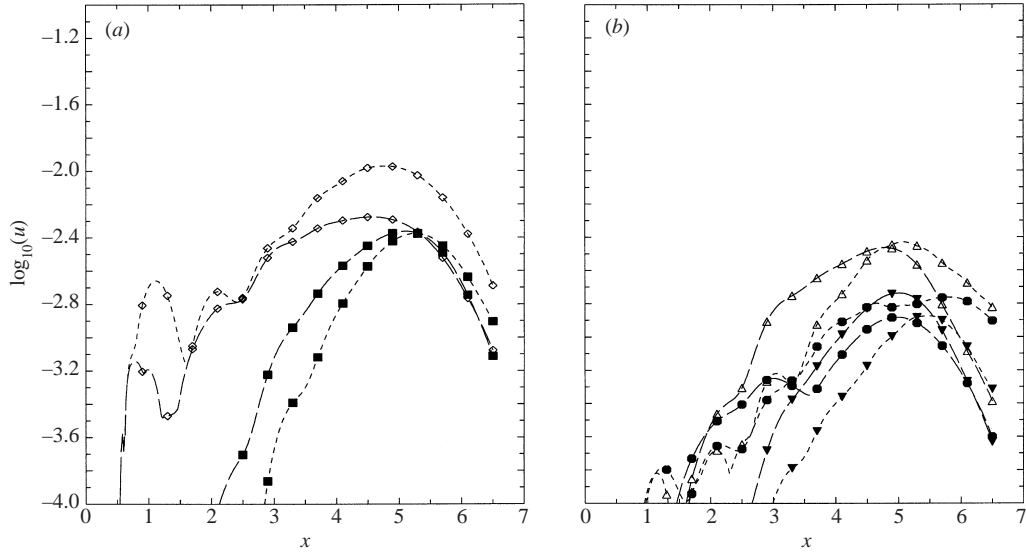


FIGURE 18. Case TS-NL-1: amplitudes of TS-disturbances with spanwise wavenumber $\gamma = 30k$ and (a) frequency $F = 0.9$ (---) and $F = 1.1$ (—); the curves are for $k = 2$ (\diamond), $k = 6$ (\blacksquare); (b) frequency $F = 0.8$ (---) and $F = 1.2$ (—); the curves are for $k = 0$ (\bullet), $k = 4$ (\triangle), $k = 8$ (\blacktriangledown).

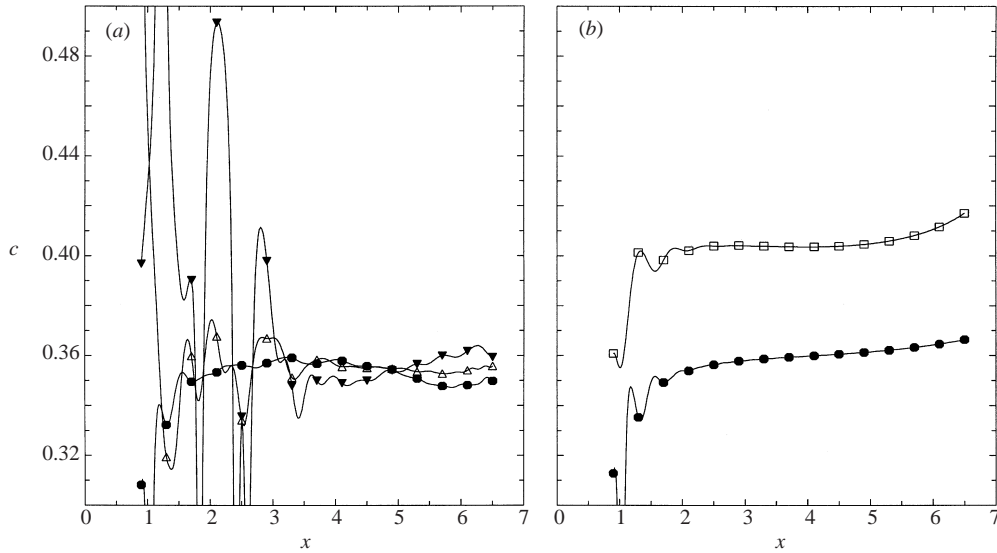


FIGURE 19. (a) Case TS-NL-1: phase velocity of TS-disturbances with frequency $F = 1$ and spanwise wavenumber $\gamma = 30k$. The curves are for $k = 0$ (\bullet), $k = 4$ (\triangle), $k = 8$ (\blacktriangledown), at $y = 0.0126$. (b) As (a) but case TS-ref. The curves are for $k = 0$ (\bullet) (two-dimensional wave), $k = 1$ (\square) (three-dimensional wave).

of the phase velocity involves computing the ratio of two very small numbers, making it very sensitive to any spurious disturbances. Hence, the contribution of other nonlinearly generated waves can easily overwhelm the phase calculation of the TS-waves. However, downstream of $x = 3.5$, the curves are sufficiently smooth to allow a useful interpretation. They show that TS-disturbances with frequency $F = 1$

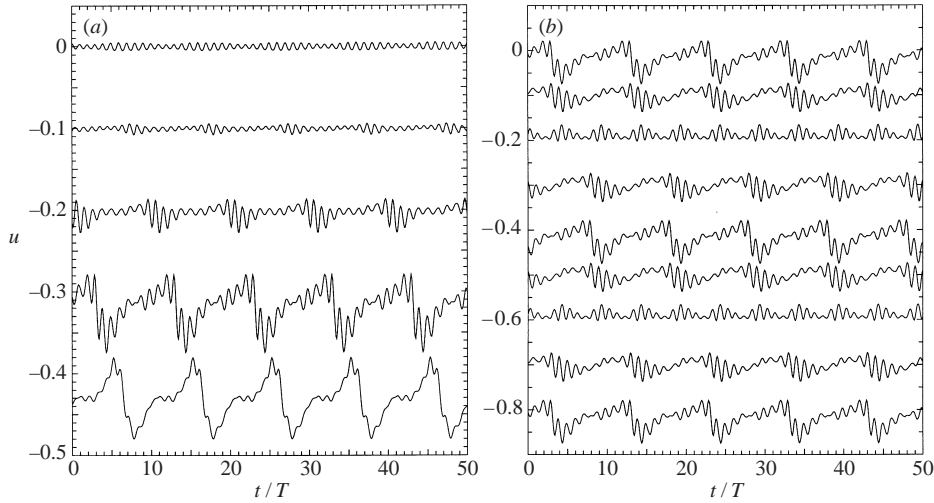


FIGURE 20. (a) Case TS-NL-1: u plotted vs. t/T , for several streamwise locations x , in the plane $z = 0$. Each curve is taken at the respective y location of maximum amplitude. The curves are, from top to bottom, at $x = 1.3, x = 2.5, x = 3.7, x = 4.9$ and $x = 6.1$. A vertical offset of 0.1 corresponds to $u = 0.1$. (b) As (a) but at $x = 4.9$ for several spanwise locations z . Top curve at $z = 0$, bottom curve at $z = 0.10472$, z -increment between consecutive curves is 0.01309.

have roughly the same phase velocity as the linear two-dimensional wave. This is in contrast to the linear reference case, plotted in figure 19(b), where the oblique wave with $k = 1$ has a significantly higher phase velocity than the two-dimensional wave. Thus, the nonlinearly generated oblique waves appear to be phase locked to the two-dimensional wave.

So far, the amplitude and phase velocity plots have provided information about the evolution of the TS-disturbances in frequency–wavenumber space. Additional insight into the nature of the disturbance waves can be gained by considering their evolution in physical (x, y, z) space and in time. Time signals $u(t)$ of the TS-disturbances at different x locations are plotted in figure 20(a). These curves correspond to the curves in figure 15. The total flow would be a superposition of the respective curves in both figures, added to the steady Blasius flow. In figure 20(b), time signals $u(t)$ are plotted at $x = 4.9$, at different spanwise locations. The top curve in figure 20(b), at $z = 0$, corresponds to the fourth curve in figure 20(a). From the curves in figure 20 it is readily apparent that the different Fourier modes seen in the amplitude plots correspond to an amplitude modulation of the original TS-wave.

A comparison with the instantaneous velocity profiles $u(y, z)$ of the K-mode in figure 14 reveals that the strongest fluctuations of the TS-disturbances coincide with localized regions of negative u -velocity of the K-mode near the wall, i.e. with a (locally) thickened boundary layer. Take, for example, the top curve at $z = 0$ in figure 20(b). The strongest fluctuations occur around $t/T = 3.5$ (modulo 10), whereas a period of relative calm occurs around $t/T = 8.5$. On the other hand, the situation is reversed at $z = 0.05236$, the fifth curve in figure 20(b). Figure 14 shows that at $t/T = 3.5$, the K-mode u -velocity is negative near the wall around $z = 0$ and attains a (positive) maximum around $z = 0.05236$, while the maxima/minima are reversed at $t/T = 8.5$. It is known from linear stability theory that increasing the boundary layer slope at the wall stabilizes a flow, while decreasing the slope destabilizes the flow. Furthermore, figure 15 shows that the u -velocity profiles have an inflection point over some range

of z and t , which may further increase the instability of the flow. These observations suggest the following explanation for the amplitude modulation of the TS-wave:

The time scales of the low-frequency K-mode and of the high-frequency TS-wave are an order of magnitude apart. Thus, the K-mode can be superimposed onto the steady Blasius boundary layer and act as a new, time-dependent base flow for the TS-wave. On the fast time scale of the TS-wave, the new base flow is steady, with the time entering as a parameter. TS-waves that propagate in a region (locally in space and time) of negative u of the K-mode would thus experience a more unstable base flow than the mean flow and be more amplified. On the other hand, those TS-waves that propagate in a local region of positive u of the K-mode would experience a more stable base flow, and be less amplified. Since the K-mode is periodic in z and t and propagates in x , the change of the local stability characteristics causes the formation of three-dimensional TS-wavepackets from an initially two-dimensional TS-wavetrain. The three-dimensional wavepackets are centred around the forcing-frequency $F = 1$ of the two-dimensional wavetrain, with amplitude and phase modulation (at fixed t) in both x and z . This transient nature of the flow is, of course, lost in the ensemble averaging typically performed in experiments, and in the Fourier amplitude of the two-dimensional wave. In fact, the steady, two-dimensional mean flow is more stable than the Blasius flow, due to the momentum transfer from the free stream to the wall induced by the K-mode. As a result, the amplitude of the two-dimensional TS-wave, averaged over t and z , is 58% lower than the amplitude of the linear reference case in §4.1. On the other hand, the maximum velocity fluctuation of the wavepackets plotted in figure 20(b) corresponds to an amplitude that is 107% higher than the reference value. Such high-amplitude wavepackets may well be precursors of turbulent spots.

5.2. Multiple wavenumber excitation of the K-mode

Analogous to the simulation in the previous section, a two-dimensional TS wave was added to the the K-mode flow from case NL-mult in §4.4. The parameters for the generation of the two-dimensional TS wave were the same as in §5.1. This calculation will be referred to as case ‘TS-NL-mult’. After the calculation, the K-mode flow computed in §4.4 was subtracted to yield the TS-disturbances.

Amplitude curves of TS-disturbances with frequency $F = 1$ are plotted in figure 21. Because of the more broad-band nature of the K-mode spectrum (see §4.4), there are more possibilities for nonlinear interactions. Thus, more spanwise Fourier modes have significant amplitudes here than in the previous section. However, the amplitude curves of those modes which are present both in the previous calculation and in this calculation are almost identical. Hence, the major contribution of the additional spanwise modes is the excitation of a more broad-band disturbance spectrum.

5.3. Transition

In this section, the calculation of §5.2 is repeated, with the forcing amplitude of the two-dimensional TS-wave increased to $\hat{v} = 2 \times 10^{-3}$. This simulation will be referred to as case ‘TS-trans’. The amplitude increase had a profound impact on the resulting flow: in the previous calculations, the amplitudes of the TS-disturbances attained a maximum near $x = 5$ and decayed thereafter. In this calculation, amplitude growth did not subside. Instead, transition to turbulence started at $x = 4$. Since the computational grid was too coarse to properly resolve a fully turbulent flow, the integration domain had to be shortened to $x_{max} = 6.1$, with the buffer domain starting at $x_B = 4.76$. Further downstream, the insufficient spatial resolution caused numerical instability.

Amplitude curves of the resulting TS-disturbances with frequency $F = 1$ are plotted

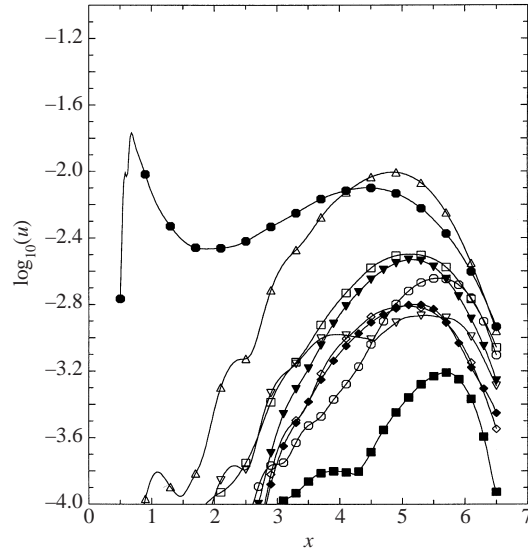


FIGURE 21. Case TS-NL-mult: amplitudes of TS-disturbances with frequency $F = 1$ and spanwise wavenumber $\gamma = 30k$. The curves are for $k = 0$ (\bullet), $k = 1$ (\square), $k = 2$ (\diamond), $k = 3$ (∇), $k = 4$ (\triangle), $k = 5$ (\circ), $k = 6$ (\blacksquare), $k = 7$ (\blacklozenge), $k = 8$ (\blacktriangledown).

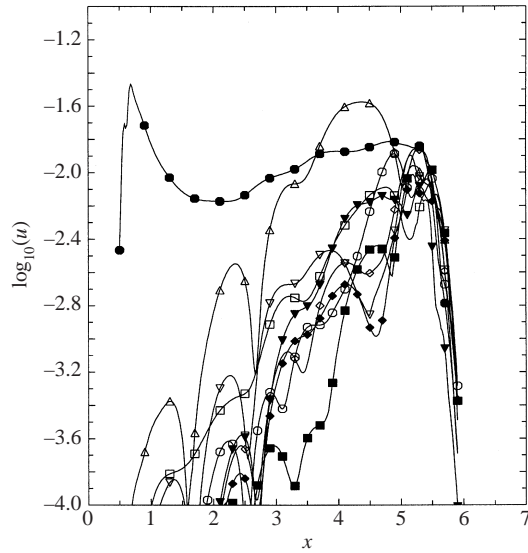


FIGURE 22. Case TS-trans: amplitudes of TS-disturbances with frequency $F = 1$ and spanwise wavenumber $\gamma = 30k$. The curves are for $k = 0$ (\bullet), $k = 1$ (\square), $k = 2$ (\diamond), $k = 3$ (∇), $k = 4$ (\triangle), $k = 5$ (\circ), $k = 6$ (\blacksquare), $k = 7$ (\blacklozenge), $k = 8$ (\blacktriangledown).

in figure 22. Note that even though disturbances are artificially damped in the buffer domain downstream of $x_B = 4.76$, the amplitudes continue to grow as far downstream as $x = 5.5$, a sign of the strong disturbance growth associated with transition.

The streamwise development of the TS-disturbance fluctuations is illustrated in figure 23. The scale of the ordinate axis is reduced by a factor of two relative to figure 20(a), proportional to the increased forcing amplitude. Thus, the top curve

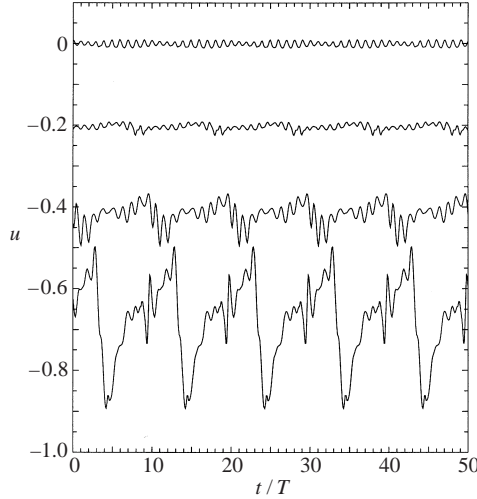


FIGURE 23. Case TS-trans: TS-disturbances u plotted vs. t/T , for several streamwise locations x , in the plane $z = 0$. Each curve is taken at the respective y location of maximum amplitude. The curves are, from top to bottom, at $x = 1.3$, $x = 2.5$, $x = 3.7$ and $x = 4.9$. A vertical offset of 0.1 corresponds to $u = 0.1$.

of figure 23, at $x = 1.3$, appears identical to the top curve of figure 20(a). Further downstream, however, significant differences appear, and the signal at $x = 4.9$ is substantially different from that of the previous calculation. The maximum fluctuation at the last x location corresponds to a u -amplitude of 20%, which is on the order of the K-mode fluctuations. Such a magnitude of u suggests consideration of the amplitudes of the combined disturbance flow (K-mode + TS-wave), instead of the TS-disturbances only. This allows an evaluation of the nonlinear feedback of the TS-wave onto the K-mode.

The amplitudes of disturbances with frequency $F = 0.1$ are plotted in figure 24. Downstream of $x = 3.5$, all amplitude curves except for mode $F = 0.1$, $k = 2$ deviate substantially from the corresponding curves in §4.4, showing strong growth up to $x = 5.5$. The u r.m.s.-amplitude is plotted in figure 25. Up to $x = 4$, the amplitude curve is very similar to those in figure 11. A minor difference is that the curve here scales as $x^{0.55}$, which is slightly closer to the experimental results than the curve in the previous section. This indicates that the presence of the high-amplitude TS-wave lowers the amplification rate of the K-mode. Downstream of $x = 4$, the r.m.s. disturbance level rises rapidly, another sign of transition to turbulence.

Time signals of the combined disturbance flow $u(t) = u_{TS} + u_{Kleb}$ are plotted in figure 26. In the top curve, at $x = 1.3$, the superposition of the TS-wave and the K-mode is easily recognizable. The next two curves, at $x = 2.5$ and $x = 3.7$, still resemble the sawtooth waves of figure 13. The last curve however, at $x = 4.9$, is qualitatively very different from that of the K-mode without the TS-wave. Time signals $u(t)$ at $x = 4.9$, at different z -stations, are plotted in figure 27(a). Time signals $u(t)$ near the streamwise maximum of the disturbance amplitudes, at $x = 5.38$, are plotted in figure 27(b). The fourth curve from the top, at $z = 0.03927$, shows velocity peaks at $t/T = 10$ (modulo 10). On the other hand, the sixth curve, at $z = 0.06545$, shows the strongest fluctuations at $t/T = 5$. In the other curves, fluctuation maxima occur at both $t/T = 5$ and $t/T = 10$. These local fluctuations can be interpreted as incipient turbulent spots.

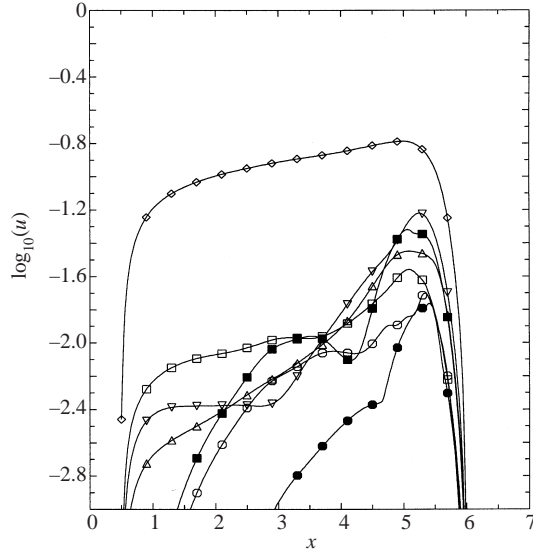


FIGURE 24. Case TS-trans: amplitudes of disturbances with frequency $F = 0.1$ and spanwise wavenumber $\gamma = 30k$. The curves are for $k = 0$ (\bullet), $k = 1$ (\square), $k = 2$ (\diamond), $k = 3$ (∇), $k = 4$ (\triangle), $k = 5$ (\circ), $k = 6$ (\blacksquare).

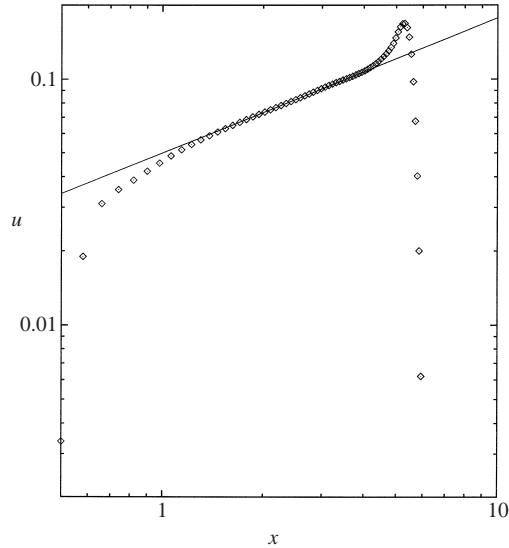


FIGURE 25. Case TS-trans: root-mean-square disturbance $u_{rms}(x)$. The straight line is $\propto x^{0.55}$.

A better understanding of the first fluctuation maximum, at $t/T = 5$, can be gained from the three-dimensional isocontours of the total spanwise vorticity $\omega_{z,B} + \omega_{z,Kleb} + \omega_{z,TS}$ plotted in figure 28. These plots show two different types of structures. The long, narrow vorticity ‘tubes’ at $z = 0$, $z = 0.10472$ and $z = 0.20944$ are associated with the K-mode. Hence, their dominant spanwise scale is $\gamma = 60$, i.e. $\lambda_z = 0.10472$. The other set of structures are vorticity ‘tongues’ centred at $z = 0.10472$, with a spanwise wavelength $\lambda_z = 0.20944$, corresponding to $\gamma = 30$. The shape of these vorticity ‘tongues’ is typical of the vorticity structure associated with a Lambda-vortex,

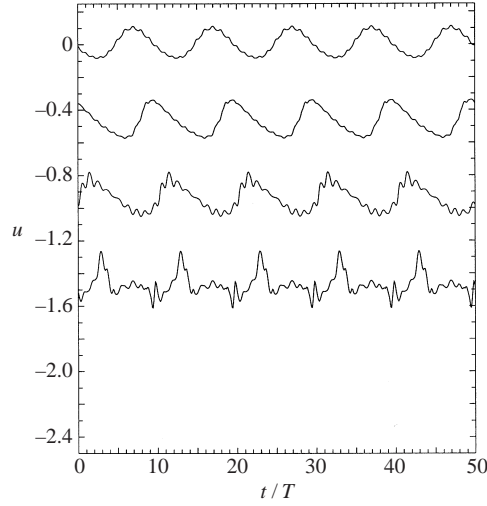


FIGURE 26. Case TS-trans: combined disturbance $u_{TS} + u_{Kleb}$ plotted vs. t/T , for several streamwise locations x , in the plane $z = 0$. Each curve is taken at the respective y location of maximum amplitude. The curves are, from top to bottom, at $x = 1.3$, $x = 2.5$, $x = 3.7$ and $x = 4.9$. A vertical offset of 0.5 corresponds to $u = 0.5$.

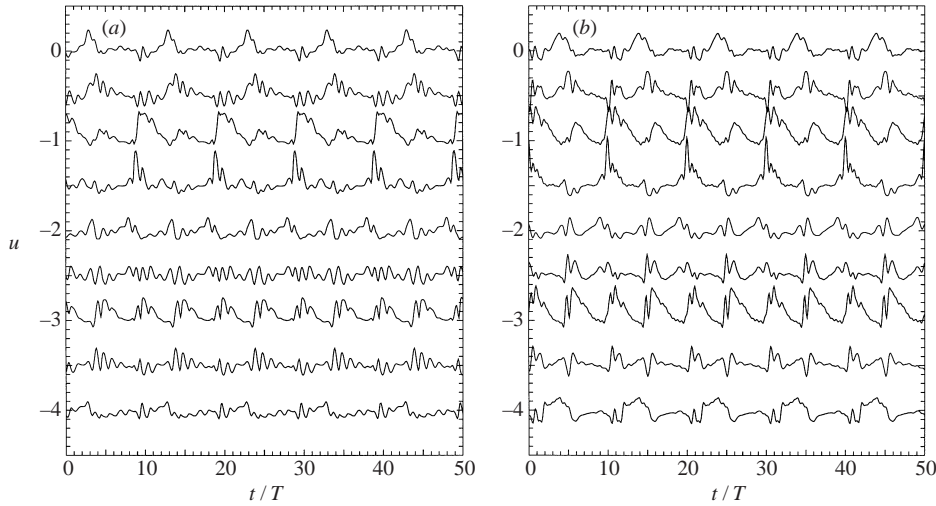


FIGURE 27. Case TS-trans: combined disturbance $u_{TS} + u_{Kleb}$ plotted vs. t/T , at (a) $x = 4.9$ and (b) $x = 5.38$, for several spanwise locations z . Each curve is taken at the respective y location of maximum amplitude. Top curve at $z = 0$, bottom curve at $z = 0.10472$, z -increment between consecutive curves is 0.01309. A vertical offset of 0.5 corresponds to $u = 0.5$.

characteristic of the fundamental breakdown to turbulence, see Rist & Fasel (1995). Hence, the breakdown of this wavepacket appears to be caused by a resonance between the two-dimensional TS-wave and an oblique wave with $\gamma = 30$. Further evidence that the fluctuation peak near $t/T = 5$ in figure 27(b) is indeed due to a fundamental breakdown is given by the three-dimensional isocontours of the streamwise vorticity ω_x , plotted in figure 29. As discussed before, the ω_x -vorticity of the K-mode is very small. Hence, the K-mode is not visible in these plots. TS-waves, on the other hand, and the Lambda-vortex associated with the fundamental

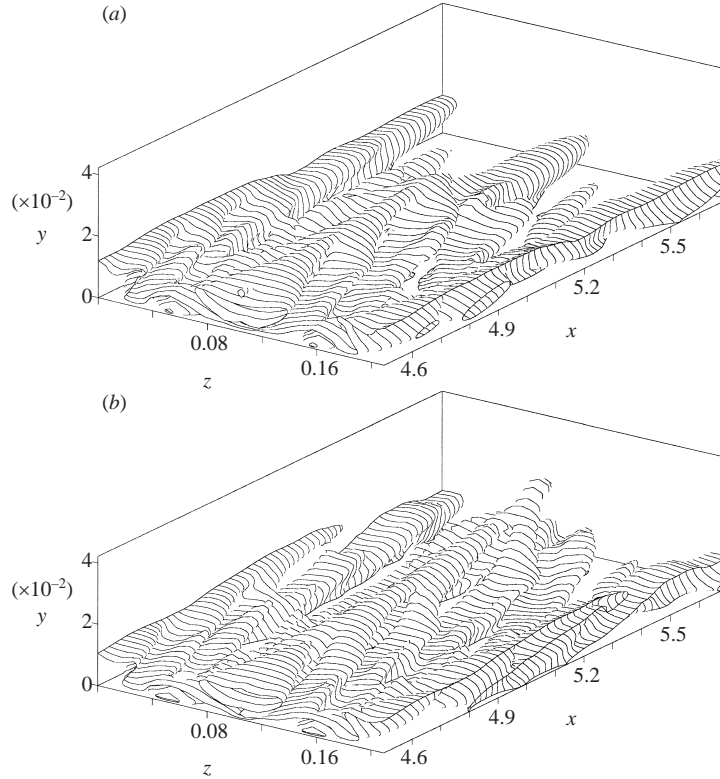


FIGURE 28. Case TS-trans: contours of constant total vorticity $\omega_{zT} = 50$ at (a) $t/T = 4$ and (b) $t/T = 5$. View from upstream.

breakdown do have a sizeable ω_x -component. This fact is reflected in the shape of the ω_x -isosurfaces, which are indicative of a Lambda-vortex.

The interpretation of the second fluctuation peak in figure 27(b), near $t/T = 10$, follows that of the first one. The events associated with this wavepacket are much more energetic and they occur a bit farther upstream. The ω_z isocontours are plotted in figure 30. The long vorticity tubes of the K-mode are now offset by 0.05236 in the spanwise direction relative to those in figure 28. The reason for the offset is the phase shift of the K-mode due to the time delay of one half-period between the two fluctuation maxima. Another important difference is that there are now two Lambda-vortices, aligned with the ω_z -tubes of the K-mode. Apparently, the breakdown of this second wavepacket is due to a resonance between the two-dimensional TS-wave and an oblique wave with $\gamma = 60$, i.e. half the spanwise wavelength of the breakdown of the first wavepacket. The corresponding ω_x isocontours are plotted in figure 31. These plots confirm the shorter spanwise scale of this breakdown.

The numerical simulation demonstrates how the interaction between a time-harmonic, low-frequency free-stream perturbation and a time-harmonic, high-frequency, two-dimensional TS-wave leads to intermittent transition via a fundamental breakdown of TS-wavepackets. The wavepackets are narrow in the spanwise direction, with the lateral scale imposed by the K-mode. This agrees with the experimental observations of Kendall (1985, 1992). Also, there appears to be a competition between two distinct fundamental resonances leading to the breakdown of the TS-wavepackets:

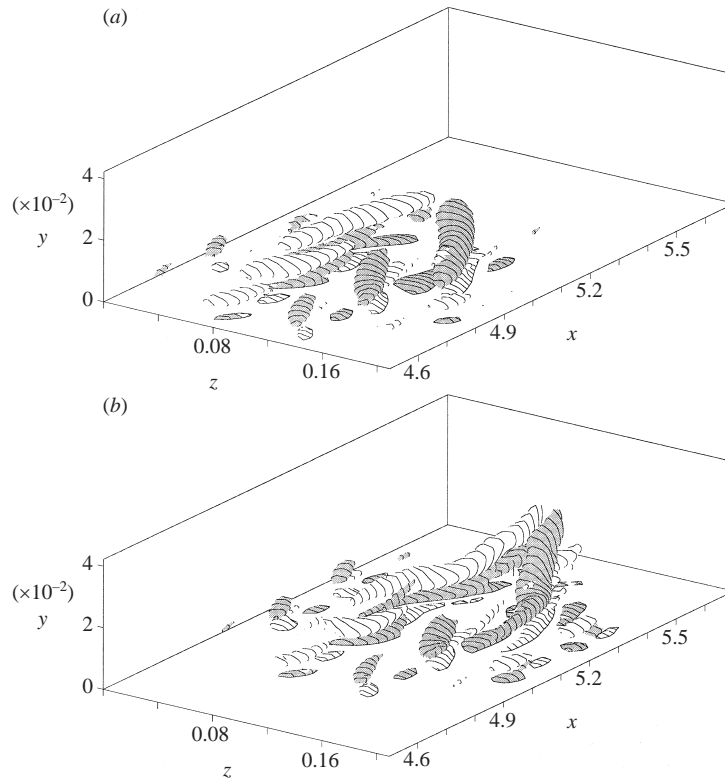


FIGURE 29. Case TS-trans: contours of constant vorticity $\omega_x = \pm 10$ at (a) $t/T = 4$ and (b) $t/T = 5$. View from upstream. Shaded surfaces indicate negative vorticity.

the more energetic one occurs on the narrow spanwise scale $\gamma = 60$ imposed by the K-mode; the second breakdown, however, is due to a resonance on the larger scale $\gamma = 30$, which is closer to that of a fundamental resonance in a clean Blasius boundary layer without the K-mode. One can expect that a more broad-band disturbance spectrum would give rise to more possible resonances, increasing the likelihood of transition at a lower Reynolds number.

A key word here is intermittency. In the numerical simulation, the low-frequency periodicity of the K-mode is clearly defined. Thus, it is rather easy to trace the developments that lead to transition, and to distinguish between the two different instances of wave-packet breakdown that occur during every period of the K-mode. In experiments, on the other hand, the frequency and wavenumber spectrum of the disturbances is more broadband. Hence, there is no distinct overall periodicity that could be exploited in measurements and in flow-visualizations. To the contrary, the band-pass filtering and ensemble averaging usually performed on experimental data obscures the crucial role that the K-mode plays in the spanwise and timewise modulation and amplification of TS-waves. Thus, narrow wavepackets appear in a seemingly random fashion, with growth and spreading rates that are significantly different from those (ensemble-averaged) of artificially induced wavepackets. As a result, to date it has been impossible to demonstrate in experiments a causal relation between the K-mode, TS-waves, and transition. There is clearly a need to perform experiments with a controlled introduction of K-mode-type disturbances and TS-

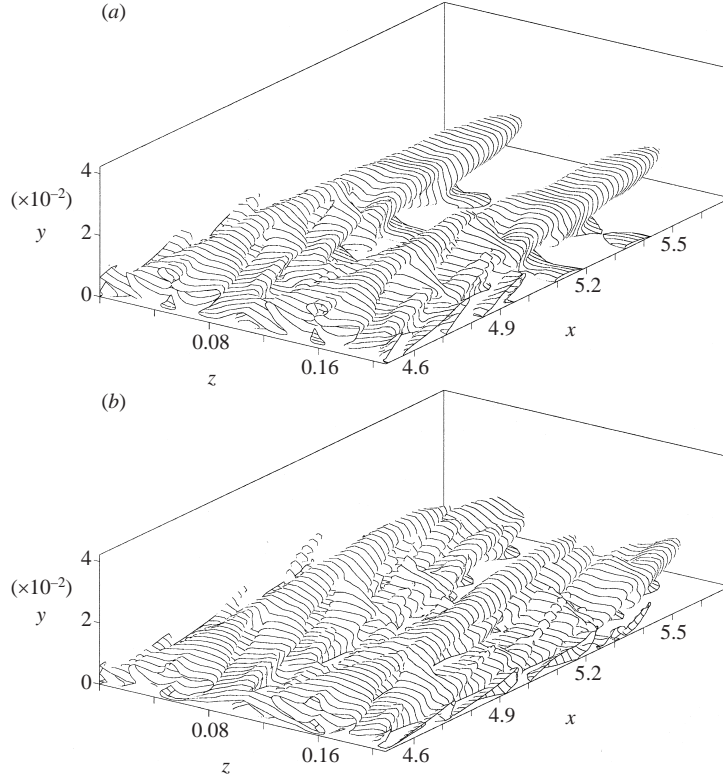


FIGURE 30. Case TS-trans: contours of constant total vorticity $\omega_{xT} = 100$ at (a) $t/T = 9$ and (b) $t/T = 10$. View from upstream.

waves to confirm (or disprove) the transition mechanism established by the present numerical simulations.

In addition to the calculations presented here, several other calculations were performed to verify the relevance of the above results. In those calculations, different fundamental spanwise wavenumbers γ_1 , disturbance spectra $amp(f, k)$, and amplitudes were used. The results of those calculations showed that, for a given r.m.s.-amplitude of the K-mode, a more broad-band spectrum of the K-mode reduced the threshold amplitude of the TS-wave necessary to trigger transition. This was expected in light of the results in §§ 5.1 and 5.2. However, the mechanism remained the same: transition was always a result of fundamental resonance. No indication of subharmonic resonance was observed.

6. Summary

In this work, direct numerical simulations (DNS) of the Navier–Stokes equations were used to investigate the role of the K-mode in laminar–turbulent transition in a flat-plate boundary layer. To model the effects of free stream turbulence, volume forces in the free stream close to the leading edge of the plate are used to generate low-frequency vortices outside the boundary layer. The response of the boundary layer to these free-stream vortices in the numerical simulations was found to agree qualitatively and quantitatively with the response of boundary layers to free-stream turbulence in experiments. This remarkable agreement validates the numerical model

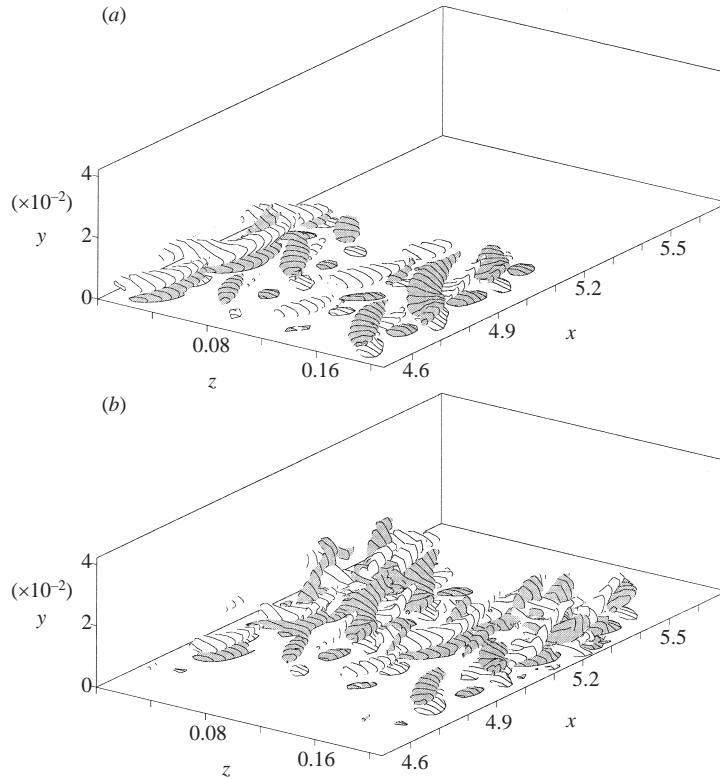


FIGURE 31. Case TS-trans: contours of constant vorticity $\omega_x = \pm 10$ at (a) $t/T = 9$ and (b) $t/T = 10$. View from upstream. Shaded surfaces indicate negative vorticity.

used in this work. The results of the numerical simulations provide substantial insight into the nature of the K-mode. The main results can be summarized as follows:

(i) The boundary layer response to the excitation by free-stream turbulence is concentrated in a narrow band of wavenumbers and frequencies. Specifically, the fairly universal spanwise scale of the K-mode fluctuations, measured in numerous experiments in different facilities, appears to be an intrinsic scale of the boundary layer.

(ii) Due to the nature of the boundary layer receptivity, it is not necessary to force a broad-band spectrum of the turbulence in the free stream to obtain the key characteristics of the K-mode. The calculations in this work showed that the forcing of a single disturbance component in the free stream suffices to obtain the proper scaling of the fluctuations inside the boundary layer.

(iii) The preferred spanwise scale of the disturbances is similar for linear and for nonlinear, high-amplitude fluctuations. The streamwise growth and the wall-normal scaling of the velocity profiles, however, are dependent on the amplitude. The growth rates and $u(y)$ profiles of linear disturbances with the frequency selected here, $F = 0.1$, are substantially different from those measured in experiments. On the other hand, nonlinear disturbances with large amplitudes similar to those measured in experiments exhibit the proper scaling in both x and y . Hence, due to its high amplitude, the characteristics of the K-mode appear to be intrinsically nonlinear.

(iv) The low values of ω_x , compared to ω_y and ω_z , indicate that the low-frequency

fluctuations associated with the K-mode are not streamwise vortices. Rather, they are essentially spanwise variations of the boundary layer thickness.

After establishing the validity of the numerical model for the K-mode, the interaction between the K-mode and a TS-wave was investigated. A suction/blowing slot at the wall was used to introduce a time-harmonic, two-dimensional TS-wave into the boundary layer, in addition to the K-mode discussed above. The results of these simulations lead to the following interpretation of the interaction between the K-mode and a Tollmien–Schlichting wave:

(i) The low-frequency, high-amplitude fluctuations of the K-mode, added to the steady mean flow, form a new ‘base flow’ for the high-frequency TS-waves. Due to the nature of the K-mode, this new base flow is periodic in z and t .

(ii) A locally positive u -velocity of the K-mode, corresponding to a thinning of the boundary layer, stabilizes the local flow, while a locally negative u -velocity, i.e. a thicker boundary layer, destabilizes the flow.

(iii) Due to the periodic change of the boundary layer stability in z and t , an initially two-dimensional TS-wavetrain undergoes differential amplification as it travels downstream, evolving into three-dimensional wavepackets.

(iv) When the fluctuations of a wavepacket are sufficiently strong, a fundamental-resonance Floquet instability sets in and triggers the breakdown of the wavepacket into a turbulent spot. However, this process is not unique. In the numerical simulation there is a competition between two distinct fundamental resonances, associated with different spanwise wavenumbers. One can expect that the broadband wavenumber spectrum of a typical experiment would give rise to even more possible resonances. The crucial point appears to be that the route to transition is that of a fundamental resonance.

Thus, in the proposed mechanism the presence of the K-mode modifies the classical transition mechanisms of linear and secondary instability, rather than introducing a new instability. In the end, transition is still caused by the amplification and breakdown of TS-waves.

This paper is based on the PhD thesis by Hubert L. Meitz, supervised by the author. The author is grateful to H.L.M. for his excellent work. The author would also like to thank Steven Crow, James Kendall, and Edward Kerschen for many valuable comments. This work was supported by the Office of Naval Research under contract number N00014-91-J-1787 and by NASA-Langley under contract number NAG 1-1422.

REFERENCES

- ARNAL, D. & JUILLEN, J. C. 1978 Contribution expérimentale à l'étude de la receptivité d'une couche limite laminaire à la turbulence de l'écoulement general. *ONERA Rap. Tech.* 1/5018 AYD, June 1978.
- BERTOLOTTI, F. 1993 Vortex generation and wave–vortex interaction over a concave plate with roughness and suction. *ICASE Rep.* 93-101.
- BOIKO, A. V., WESTIN, K. J. A., KLINGMANN, B. G. B., KOZLOV, V. V. & ALFREDSSON, P. H. 1994 Experiments in a boundary layer subjected to free-stream turbulence. Part 2. The role of TS-waves in the transition process. *J. Fluid Mech.* **281**, 219–245.
- CRAIK, A. D. D. 1971 Nonlinear resonant instability in boundary layers. *J. Fluid Mech.* **50**, 393–413.
- CROW, S. C. 1966 The spanwise perturbation of two-dimensional boundary layers. *J. Fluid Mech.* **24**, 153–164.
- FASEL, H., RIST, U. & KONZELMANN, U. 1990 Numerical investigation of the three dimensional development in boundary layer transition. *AIAA J.* **28**, 29–37.

- GASTER, M. & GRANT, I. 1975 An experimental investigation of the formation and development of a wave packet in a laminar boundary layer. *Proc. R. Soc. Lond. A* **347**, 253–269.
- GOLDSTEIN, M. E. & LEIB, S. J. 1993 Three-dimensional boundary-layer instability and separation by small-amplitude streamwise vorticity in the upstream flow. *J. Fluid Mech.* **246**, 21–41.
- GOLDSTEIN, M. E., LEIB, S. J. & COWLEY, S. J. 1992 Distortion of a flat-plate boundary-layer by free-stream vorticity normal to the plate. *J. Fluid Mech.* **237**, 231–260.
- HERBERT, T. 1988 Secondary instability of boundary layers. *Ann. Rev. Fluid Mech.* **20**, 487–526.
- KENDALL, J. M. 1985 Experimental study of disturbances produced in a pre-transitional laminar boundary layer by weak freestream turbulence. *AIAA Paper* 85-1695.
- KENDALL, J. M. 1990 Boundary layer receptivity to freestream turbulence. *AIAA Paper* 90-1504.
- KENDALL, J. M. 1992 Boundary layer receptivity to weak freestream turbulence. Notes on Figures Presented at T.S.G. Meeting, Big Sky, July 13, 1992.
- KLEBANOFF, P. 1971 Effect of freestream turbulence on the laminar boundary layer (Abstract). *Bull. Am. Phys. Soc.* **10**, No. 11.
- KLEBANOFF, P. S. & TIDSTROM, K. D. 1959 Evolution of amplified waves leading to transition in a boundary layer with zero pressure gradient. *NASA TN D* 195.
- KLOKER, M., KONZELMANN, U. & FASEL, H. 1993 Outflow boundary conditions for spatial Navier–Stokes simulations of transitional boundary layers. *AIAA J.* **31**, 620–628.
- MEITZ, H. L. 1996 Numerical investigation of suction in a transitional flat-plate boundary layer. PhD dissertation, University of Arizona.
- MORKOVIN, M. V. 1993 Bypass-transition research: issues and philosophy. In *Instability and Turbulence in Engineering Flows* (ed. D. E. Asphis, T. B. Gatski & R. Hirsh), pp. 3–30. Kluwer.
- RIST, U. & FASEL, H. 1995 Direct numerical simulation of controlled transition in a flat-plate boundary layer. *J. Fluid Mech.* **298**, 211–248.
- WESTIN, K. J. A., BOIKO, A. V., KLINGMANN, B. G. B., KOZLOV, V. V. & ALFREDSSON, P. H. 1994 Experiments in a boundary layer subjected to free-stream turbulence. Part 1. Boundary layer structure and receptivity. *J. Fluid Mech.* **281**, 193–218.